Article

Development of an Optical System for Non-Contact Type Measurement of Heart Rate and Heart Rate Variability

Jyoti Gondane * and Meena S. Panse

Department of Electrical Engineering, Veermata Jeejabai Technological Institute (VJTI), Mumbai 400019, India; mspanse@el.vjti.ac.in
* Correspondence: jagondane@el.vjti.ac.in

Abstract: Self-mixing optical coherent detection is a non-contact measurement technique which provides accurate information about the vibration frequency of any test subject. In this research, novel designs of optical homodyne and heterodyne detection techniques are explained. Homodyne and heterodyne setups are used for measuring the frequency of the modulated optical signal. This technique works on the principle of the optical interferometer, which provides a coherent detection of two self-mixing beams. In the optical homodyne technique, one of the two beams receives direct modulation from the vibration frequency of the test subject. In the optical heterodyne detection technique, one of the two optical beams is subjected to modulation by an acousto-optics modulator before becoming further modulated by the vibration frequency of the test subject. These two optical signals form an interference pattern that contains the information of the vibration frequency. The measurement of cardiovascular signals, such as heart rate and heart rate variability, are performed with both homodyne and heterodyne techniques. The optical coherent detection technique provides a high accuracy for the measurement of heart period and heart rate variability. The vibrocardiogram output obtained from both techniques are compared for different heart rate values. Results obtained from both optical homodyne and heterodyne detection techniques are compared and found to be within 1% of deviation value. The results obtained from both the optical techniques have a deviation of less than 1 beat per minute from their corresponding ECG values.

Keywords: homodyne detection; heterodyne detection; Mach–Zehnder interferometer; acousto-optics modulator; vibrocardiogram; heart period; heart rate; heart rate variability

1. Introduction

The maximum critical cases across the world are related to chronic cardiorespiratory conditions. Demographic changes are expected to cause home monitoring approaches to take a leading role in the future treatment of such patients [1,2]. Remote monitoring technologies have gained a significant importance in the COVID-19 era. During the pandemic, the use of non-contact type techniques for the measurement of bio-parameters have increased rapidly. Although fixed-on-body electrodes are reliable and give good signal quality, there are several disadvantages of this method. The major demerit of this technique is the direct fixing of electrodes on skin, as it leads to discomfort among patients. Direct measurement on skin becomes very critical, especially in the case of infants and people with burn injuries. Therefore, the interpretation of cardiovascular signals through unobtrusive means has gained importance in recent years. A vast amount of research is available for the measurement of cardiovascular parameters, but most of the research is related to contact type measurement. There is much less clinical awareness of non-contact type optical measurement of cardiovascular parameters. There are several reasons contributing to this fact, such as the absence of a specific therapy for prognosis improvement. Furthermore, there is a lack of standardized methodology for parameter assessment due to the variability of factors, such as gender, age, medical history for illness, and drug interferences [3]. The common intention behind this development is to enable the

monitoring of cardiovascular parameters, such as heart rate (*HR*) and heart rate variability (*HRV*), in scenarios that prevent the use of conventional clinical sensors, normally requiring some sort of direct electrical (resistive) or mechanical coupling. Less variation in *HR* is not good for the health of a person. Generally, a high variability in *HR* is an indicator of good health for a person [4,5]. *HRV* provides information about the person's physical and emotional response towards any illness and stress [6]. It can provide important information about blood sugar, blood pressure, digestion, and the respiration cycle. Understanding *HRV* provides vital information about many biological systems and processes. The measurement of *HRV* is more complex than the measurement of *HR*. As *HRV* measurement involves changes in the heart period in the order of milliseconds, it requires higher degrees of accuracy than *HR*.

Optical interferometer-based detection setups are widely used in many fields, such as medicine, automation, and architecture. Optical coherent detection techniques mainly consist of homodyne and heterodyne type detection methods. S.F. Jacobs first provided the theoretical comparisons of two detection schemes [7], compared the modulation schemes of both techniques, and provided the methods of optical beating inside a Mach–Zehnder interferometer. Koukoulas et. al. presented the results of a hydrophone calibration comparison between reciprocity and interferometry [8]. The same author provided a comparison between heterodyne and homodyne interferometry in order to realize the acoustic pascal unit of acoustic pressure in water [9]. The author directly compared the two techniques used in underwater acoustics and ultrasonics in terms of acoustic pressure estimation.

More recently, laser vibrometers have been considered for the non-contact monitoring of cardiac activity from measurements performed on the chest wall. Laser Doppler vibrometer-based methods are used to perform both *HR* and *HRV* analysis, with results equivalent to ECG. Tomasini et al. demonstrated the measurement of pressure waves by means of a laser vibrometer [10]. Morbiducci U et al. used a commercial laser Doppler vibrometer for vibratory measurements at long operative distances (tens of meters) [11,12]. Lorenzo Scalise et al. proposed a protocol for monitoring cardiac activity by measuring the skin surface vibrations of the main neck vessels caused by vascular wall motion in the carotid artery [13]. The author proposed the measurement of the velocity of displacement of the skin in correspondence to the chest wall. The method is based on the optical recording of the movements of the neck by means of laser Doppler interferometry. De Melis et al. proposed a vibratory signal measurement from the chest wall and carotid [14]. Many studies have demonstrated displacement measurements with $\frac{\lambda}{2}$ (or better resolution). In this approach, scattered light from a vibrating surface is used to detect the amplitude and frequency of surface vibrations [15–17]. Many studies have demonstrated the absolute distance measurement with a self-mixing method [18–22].

The heart and lungs work together to transport oxygenated blood throughout the body. Deformation of the heart results in the generation of vibration frequencies on human skin, especially on the chest wall and the wrist. Therefore, the analysis of vibrations on the skin surface provides crucial information about the type of disorder. The movement and deformation of the heart, as well as the pulse wave traveling through the body, results in displacement and vibration of the body surface [23]. The human chest wall consists of independent mechanical components that contribute to chest wall mechanics. Optical coherent detection is one of the important techniques for measuring the frequency of vibration on a test subject. The aim of the optical sensing method proposed here is to observe the activity of the heart with an approach based on a custom-made low-cost self-mixing laser interferometer. The optical interferometer-based system directly measures the vibration frequency on human skin with a very high accuracy and temporal resolution. The coherent detection technique involves the vibration measurement by two independent optical setups, namely homodyne and heterodyne. It works on the principle of the modulation of light signal by mechanical vibrations. Measurements carried out with these techniques are non-intrusive and non-destructive. These techniques are completely contactless and are relatively precise and sensitive [24]. The detection method is called

self-mixing because the two interfering beams are obtained from the same optical source from the beam splitter [25]. The optical coherent detection technique is useful for the monitoring of the burnt patients or preterm infants.

The main contributions of this research are:

1. A novel design of a self-mixing optical homodyne and heterodyne detection setup for measuring the vibrations of chest wall or wrist position is proposed;
2. A comparison of results of homodyne and heterodyne techniques with available contact type measurement techniques, such as an electrocardiogram (ECG), is studied;
3. The feature extraction of the vibrocardiogram (VCG) signal for the monitoring of *HR* and *HRV* is obtained.

In this research paper, Section 2 describes the modulation scheme for the design of optical homodyne detection and optical heterodyne detection. Section 3 provides details about the experimental setup for the measurement of vibration on the chest wall and wrist. Section 4 analyses the results of the *HR* and *HRV* measurement. In this section, feature extraction of vibrocardiogram (VCG) waves is performed and its mapping with ECG signal is explained. Further, the results of optical homodyne and heterodyne techniques are compared based on the results. The research also provides details of the construction of the proposed optical homodyne and heterodyne setups.

2. Optical Coherent Detection Technique

The optical coherent detection techniques consist of a Mach–Zehnder interferometer or Michelson interferometer. In a Mach–Zehnder interferometer, an optical signal is divided into two parts with a beam splitter. These two beams travel a distance of L_1 and L_2 in two orthogonal arms of the interferometer and are combined at another beam coupler, as shown in Figure 1. The two signals are made to travel exact equal distances, so that the total path difference between these beams is always zero.
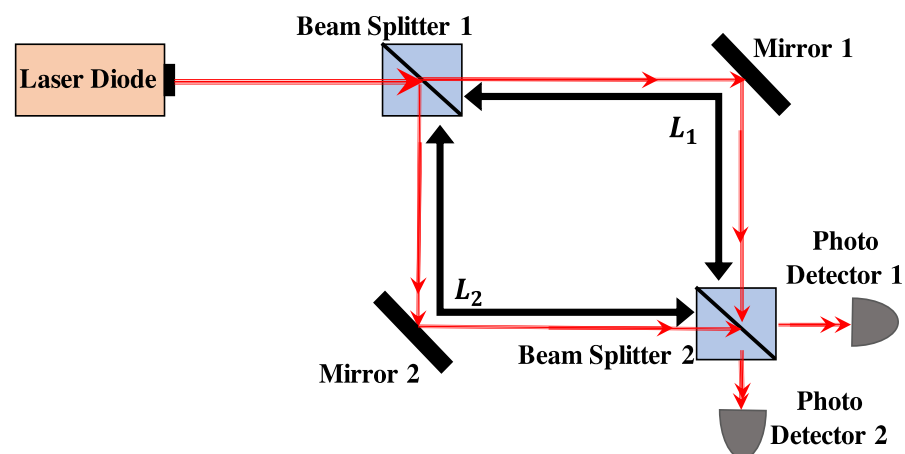

Figure 1. Mach–Zehnder Interferometer.

Mirrors M1 and M2 are used to fine tune the total path difference between the two beams. Once the path difference (i.e., $\Delta L = L_1 - L_2$) is zero, the phase difference between the two beams becomes constant or zero, as the phase difference $\Delta\varphi$ is directly proportional to the path difference [26]. The interference pattern is observed at the photo detector. The phase difference (in radians) between the two beams is given by,

$$\Delta\varphi = \frac{2\pi}{\lambda}\Delta L \tag{1}$$

If the two beams travel an equal path, the path difference between them will be either zero or constant. It will lead to a constant phase difference between the two beams [27]. The condition for constructive interference is given by,

$$\Delta L = n\lambda \quad for \; n = 0, 1, 2 \ldots \tag{2}$$

The condition of destructive interference is given by,

$$\Delta L = (n+1)\frac{\lambda}{2} \quad for \; n = 0, 1, 2 \ldots \tag{3}$$

2.1. Optical Homodyne Detection

Even the well-behaved lasers, such as the Nd:YAG laser and He: Ne laser, show frequency fluctuations due to thermal change and vibrations. One solution for this problem is to use the same laser for the local oscillator and the signal beams. This type of system is called a "homodyne" system. The main advantage of this system is its insensitivity towards frequency fluctuations when the path length of the two arms are equal. The optical homodyne detection technique requires interference of the two optical beams. The first beam is the input optical carrier signal with frequency f_s, while the second optical beam is provided by a local oscillator with frequency f_{LO}, as shown in Figure 2. The optical signal is demodulated directly to the baseband. It requires a local oscillator whose frequency matches the carrier signal and whose phase is locked to the incoming signal ($f_s = f_{LO}$). Information can be transmitted through amplitude, phase, or frequency modulation [28].
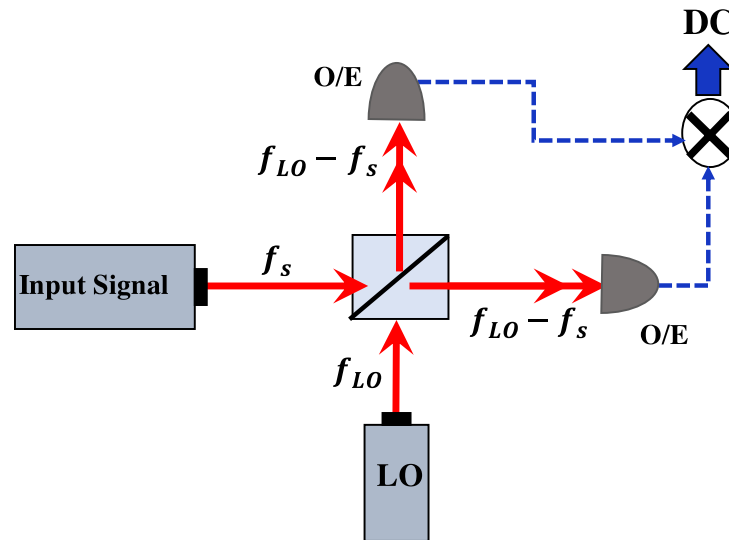

Figure 2. Optical homodyne detection.

The input carrier signal is given by,

$$E_s = A_s Exp\left[-j(\omega_s t + \Phi_s)\right] \tag{4}$$

and the local oscillator signal is given by,

$$E_{LO} = A_{LO} Exp\left[-j(\omega_{LO} t + \Phi_{LO})\right] \tag{5}$$

The output power of the photodetector is,

$$P(t) = P_s + P_{LO} + 2\sqrt{P_s P_{LO}} \cos(\omega_{IF} t + \Phi) \tag{6}$$

and the power of the modulated signal is given by,

$$P_s = \frac{A_s^2}{2} \tag{7}$$

while the power of the local oscillator signal is given by,

$$P_{LO} = \frac{A_{LO}^2}{2} \tag{8}$$

The intermediate frequency signal is given by ω_{IF}, which is the difference of the carrier signal and local oscillator signal frequency.

$$\omega_{IF} = \omega_s - \omega_{LO} \tag{9}$$

The overall phase shift observed at the detector is the difference of the phase of input carrier signal and the local oscillator signal. The overall phase shift is given by,

$$\Phi = \Phi_s - \Phi_{LO} \tag{10}$$

2.2. Heart Rate Detection with Self-Mixing Optical Homodyne Technique

The optical homodyne detection technique for *HR* detection makes use of self-mixing of the same type of frequency signal, as shown in Figure 3. The laser diode signal with frequency f_0 is split in two orthogonal arms of a Michelson interferometer by a 3 dB beam splitter. The frequency of the optical signal remains the same (f_0) in both orthogonal arms. In this case, the local oscillator signal is provided by a fixed mirror M, which reflects back the same optical signal, whose frequency is f_0. The modulated optical signal is the optical signal that is reflected from the skin surface of the human test subject. Both the local oscillator and modulated signals are obtained in two orthogonal arms of the Michelson interferometer. Optical signals travel in the two orthogonal arms and are combined at the same 3 dB splitter. In this case, both optical signals travel the same path distance in the two arms of the interferometer.
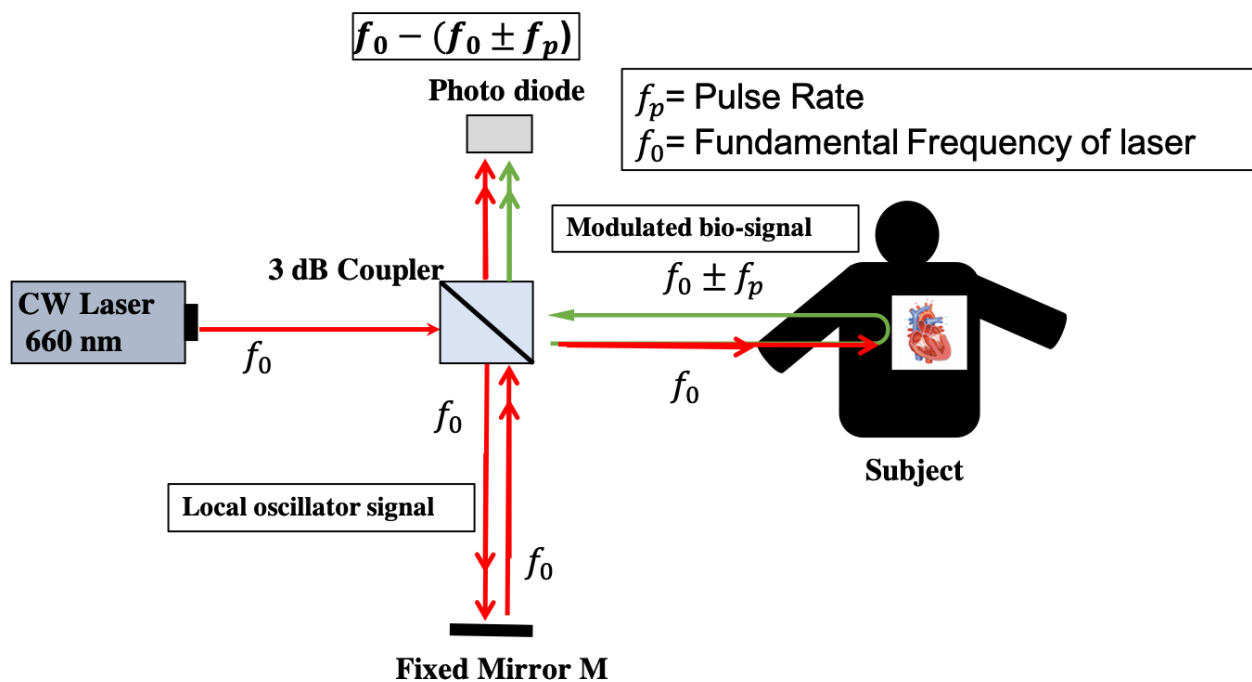

Figure 3. Self-mixing homodyne detection for heartbeat measurement.

Thus, the total path difference in the two orthogonal arms becomes zero. The zero-path difference in both orthogonal arms leads to zero phase difference between two optical signals. Therefore, the phase of the carrier signal with frequency $f_0 \pm f_p$ is matched to the local oscillator signal with frequency f_0 and the phase of both the beams are locked [29]. The Modulated bio signal is given by,

$$E_s = A_s Exp\left[-j[2\pi(f_0 \pm f_p)t + \Phi_s]\right] \tag{11}$$

The local oscillator signal is given by,

$$E_{LO} = A_{LO} Exp\left[-j[2\pi f_0 t + \Phi_{LO}]\right], \tag{12}$$

The output power of the photodetector is,

$$P(t) = P_s + P_{LO} + 2\sqrt{P_s P_{LO}} \cos(2\pi f_{IF} t + \Phi_s - \Phi_{LO}), \tag{13}$$

The intermediate frequency signal is given by f_{IF}, which is the difference of the carrier signal and the local oscillator signal frequency.

$$f_{IF} = (f_0 \pm f_p) - f_0, \tag{14}$$

The beating of the two optical signals provides the *HR* frequency (f_p) at the photo detector, which is equal to f_{IF}, i.e.,

$$f_{IF} = f_p, \tag{15}$$

The overall phase shift observed at the detector is the difference of phase of modulating bio signal (Φ_m) and phase of input optical signal (Φ_s). It is given as,

$$\Phi = \Phi_m - \Phi_s \tag{16}$$

The phase difference between both orthogonal beams is zero and constant inside the interferometer.

2.3. Optical Heterodyne Detection Technique

The optical heterodyne detection scheme consists of acousto-optic modulators (AOM) in order to generate an optical frequency shift. An acousto-optic effect is generated with an acoustic wave into a lead molybdate crystal. The acoustic wave causes a change in the refractive index, which is periodic in nature. This generates an effect analogous to a moving diffraction grating along the material, with the site spacing equal to the wavelength of the acoustic wave. An AOM cell, as shown in Figure 4, is constructed using a piezo-electric transducer to introduce the sound waves into the transparent material. It creates a diffraction grating in the material which has a spacing equal to the order of the wavelength of the acoustic wave. A piezo-electric transducer is used to create the acoustic wave into the lead molybdate crystal. In AOM, the angle of incidence satisfies Bragg's condition for constructive interference. The period of spacing created by the acoustic wave is given by $\wedge$. In order to satisfy Bragg's condition, the incident angle (θ) is given by,

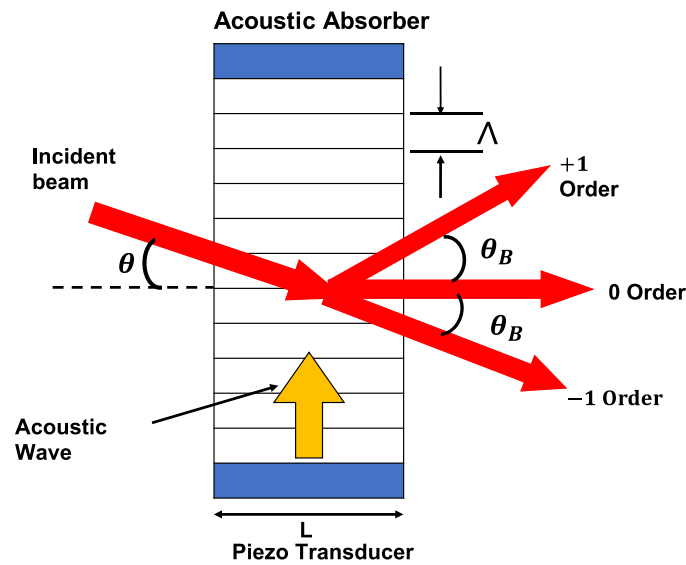$$\theta = \sin^{-1}\left(\frac{\lambda}{2n\wedge}\right) \tag{17}$$

Figure 4. Structure of AOM.

The optical heterodyne technique makes use of modulation from the AOM frequency signal, as shown in Figure 5. The input signal with frequency f_s is combined with the local oscillator signal with frequency f_{LO} by using a 3 dB beam combiner. The combined frequency of the optical signal remains the same $(f_s - f_{LO})$ in both orthogonal arms. The AOM modulates the optical signal in one arm with modulation frequency f_m. The optical beating of one signal with frequency $f_s - f_{LO} - f_m$ and the other signal with frequency $f_s - f_{LO}$ will result in the direct detection of modulation frequency f_m at the photo receiver [30].
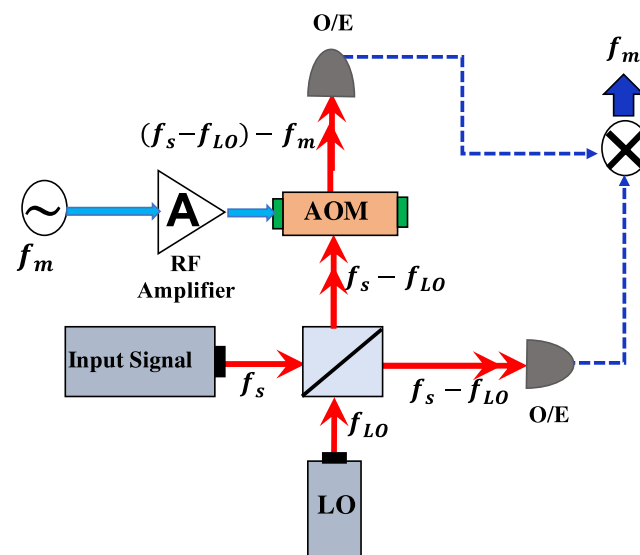

Figure 5. Optical heterodyne detection.

2.4. Heart Rate Detection with Self Mixing Optical Heterodyne Technique

The self mixing interferometer consists of a Mach–Zehnder interferometer, as shown in Figure 6. Unlike homodyne detection, the frequency of the fundamental optical signal is not same as the local oscillator signal $(f_0 \neq f_{LO})$ in heterodyne detection. Therefore, the modulation frequency f_m is detected at the receiver due to optical beating. The self-mixing optical heterodyne detection technique makes use of AOM in the test arm of the interferometer.
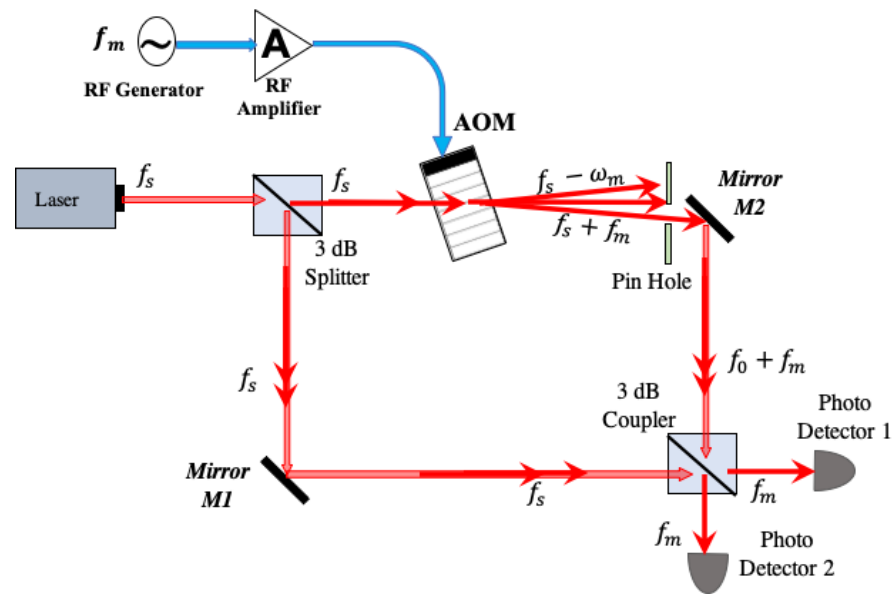
Figure 6. Self-mixing heterodyne detection with M–Z interferometer.

Figure 7 shows the detection of the *HR* signal with the self-mixing heterodyne detection scheme. The test arm of the Mach–Zehnder interferometer consists of an AOM. The optical signal first becomes modulated by the RF frequency f_m given to the AOM. Further, this signal is subjected to another modulation by reflection from the chest wall of the test subject. The chest wall vibrations are due to the *HR* frequency f_H. The optical signal after reflection from the chest wall has a frequency of $f_s \pm f_m \pm f_H$. The fundamental optical signal passes through the reference arm of interferometer. The fundamental optical signal and bio-modulated optical signal orthogonally combine at the 3 dB coupler. In this case, in both arms of the interferometer, optical signals travel the same path distance. The total path difference in the two orthogonal arms becomes zero. The zero-path difference in both orthogonal arms leads to a zero phase difference between the two signals. Therefore, the phase of the modulated signal with frequency $f_s \pm f_m \pm f_H$ is matched to local oscillator signal with frequency f_s and the phase of both the beams are locked [31].
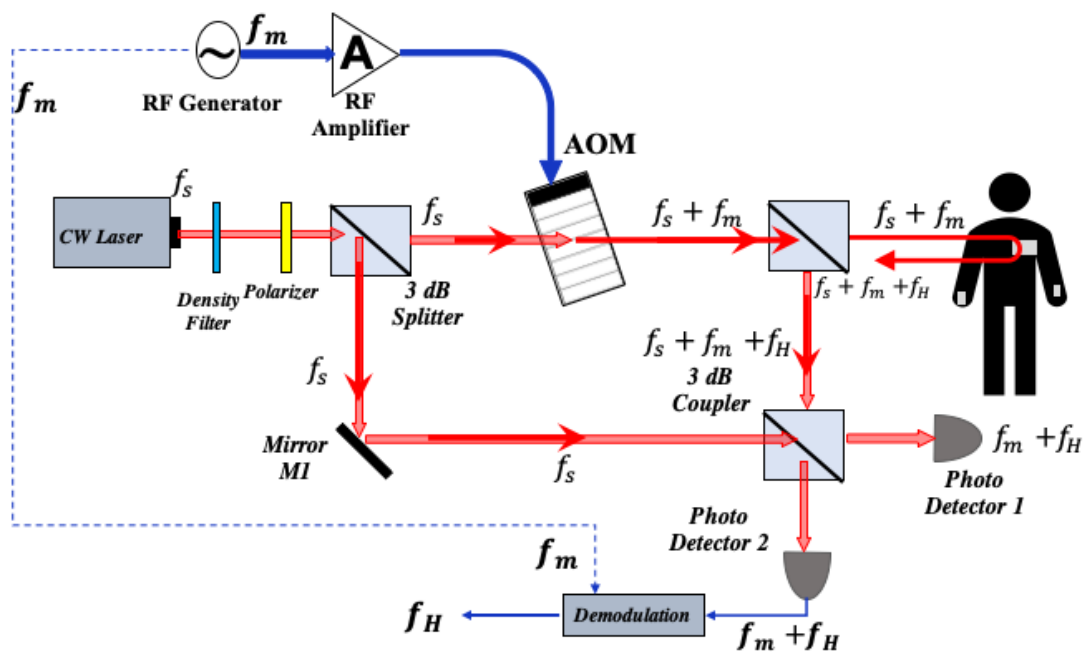

Figure 7. Self-mixing heterodyne detection with human test subject.

The modulated bio signal in the test arm of the interferometer is given by,

$$E_{s,t} = A_{s,t} Exp \left[-j[(\omega_s \pm \omega_m \pm \omega_H)t + \Phi_{s,t}] \right] \tag{18}$$

The fundamental optical signal in the reference arm of the interferometer is given by

$$E_{s,r} = A_{s,r} Exp \left[-j[\omega_s t + \Phi_{s,r}] \right] \tag{19}$$

The output power of the photodetector is given by,

$$P(t) = P_{s,t} + P_{s,r} + 2\sqrt{P_{s,t}P_{s,r}} \cos(2\pi f_{IF} t + \Phi_{s,t} - \Phi_{s,r}) \tag{20}$$

The intermediate frequency signal is given by f_{IF}, which is the difference between the frequency of the test and the reference signals.

$$f_{IF} = (f_s \pm f_m \pm f_H) - f_s \tag{21}$$

f_{IF} provides the heart frequency with the modulation frequency of AOM at the photo detector,

$$f_{IF} = f_m \pm f_H \tag{22}$$

The overall phase shift observed at the detector is the phase difference of the modulating signal in the test arm and the fundamental signal in the reference arm [32]

$$\Phi = \Phi_{s,t} - \Phi_{s,r} \tag{23}$$

3. Experimental Setup of Optical Homodyne and Heterodyne Detection

3.1. Experiment for Heart Rate Detection with Self-Mixing Optical Homodyne Technique

Thin nano film reflectors are used for reflection of the laser signal. These reflectors are mounted on the wrist and chest wall of the test subject. Due to their negligible mass, thin film reflectors vibrate with the same frequency as that of heart frequency. The thin film reflectors are prepared with gold sputtering and aluminum sputtering techniques. Thin antireflection coating on glass for optical applications are deposited by sputtering. Sputtering is a vapor phase deposition (PVD) method of thin film deposition [33]. This involves ejecting material from source onto a silicon wafer. Optical coatings are deposited in the wavelength regions between visible and far-IR. The used samples were silica substrates with thickness of 1 μm. The atomic force microscopy (AFM) image of gold-sputtered thin film nano reflector is shown in Figure 8. In order to optimize the quality of the bio-signal, a thin film reflector with an adhesive tape was placed on the chest wall. The thin film reflector increases the S/N ratio of the vibratory signal. Instead of thin film reflectors, 45% hydrating zinc oxide spray or paste on skin can also be used in order to maximize the reflection.
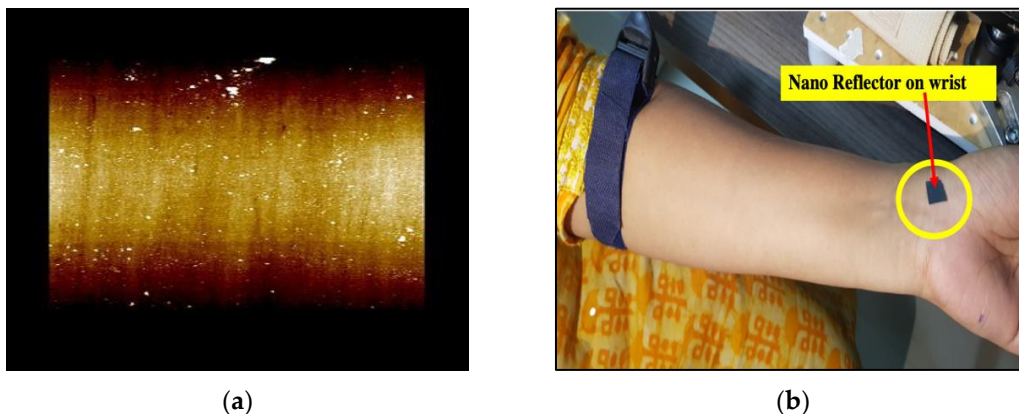

(**a**)　　　　　　　　　　　　　　　　　　　(**b**)

Figure 8. (**a**) Gold deposition process on silica substrate; (**b**) thin film reflector on wrist position.

The experiment setup of homodyne detection consisted of a laser diode, a beam splitter, mirrors, and photodetectors. The laser diode used in this setup was semiconductor AlGaInP laser with wavelength 660 nm and power 10 mW. The laser beam is split into two parts by a beam splitter. One beam travels towards the fixed mirror while other beam travels towards thin film reflector, which is fixed on the human wrist or the chest wall. Both beams after reflection from the mirrors combine at the same beam splitter and interference pattern is observed at the photodetector. A tight strip band is fixed near the elbow position so that heart pulse is properly located on the wrist. Figure 9 shows the experimental setup for homodyne detection scheme. Figure 10 shows the response of photodetector for homodyne detection. It clearly shows measurement of vibration on human wrist skin, which indicates heart frequency. The measurement of heart frequency was carried out at the chest wall position with similar results. The laser was placed at approximately 10 cm from the subject's chest wall and wrist position [34]. A low pass filter (cut off frequency ≤ 5 Hz) was placed in series with photo detector for denoising of the optical beat signal. Laser diode with power of 10 mW was used, so that no special safety measures were required. Even with low power level, a working distance of 10 m is feasible.
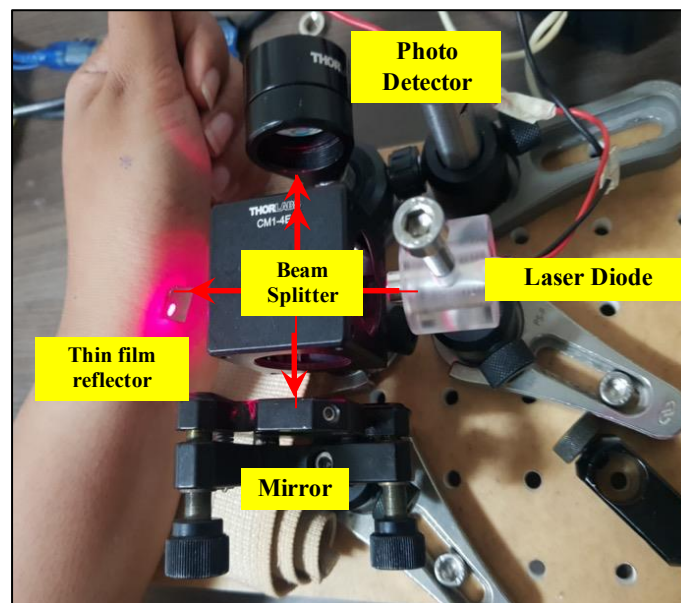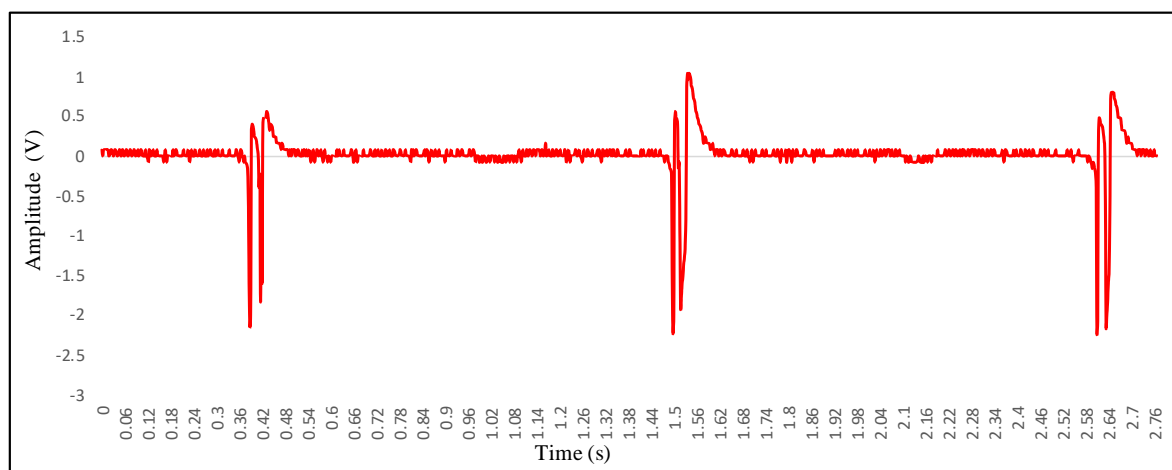

Figure 9. *HR* detection with optical homodyne technique.

Figure 10. *HR* detection on wrist position with optical homodyne technique.

3.2. Experiment of Heart Rate Detection with Self Mixing Optical Heterodyne Technique

The AOM used for this experiment was ISOMET AOM with model number 1205C-2 [35]. Table 1 shows the specifications of ISOMET AOM.

Table 1. AOM specification.

Parameter	Specification
Material	Lead molybdate
Active aperture	2 mm
Center frequency	60 MHz
Center wavelength	660 nm

An RF signal source was used to modulate the reference frequency of the actual laser beam. RF signal generator tunes the laser beam given to AOM and modulates it with various frequency range. Further, an RF amplifier was used in series with RF generator to provide high gain. RF amplifier was needed because AOM requires a minimum 25 dBm RF power as an input in order to provide modulation. The maximum gain of 32 dB can be obtained with RF amplifier. Table 2 shows the specifications of the RF generator and the RF amplifier circuit.

Table 2. Specification of RF generator and amplifier.

Parameter	Specification
RF signal generator voltage	12 V
RF signal generator output frequency	70 MHz–200 MHz
Output power RF generator	10 dBm
RF amplifier supply voltage	12 V DC
RF amplifier gain	32 dB

The optical signal produced multiple order side bands with frequency 454.5 THz $\pm$ 60 MHz. These side bands are shown in Figure 11a,b. Figure 12 shows the modulation of 660 nm laser beam with 60 MHz RF signal, where 660 nm laser corresponds to 454.5 THz frequency. Light signal was modulated by the RF signal of 60 MHz after passing through AOM [36].
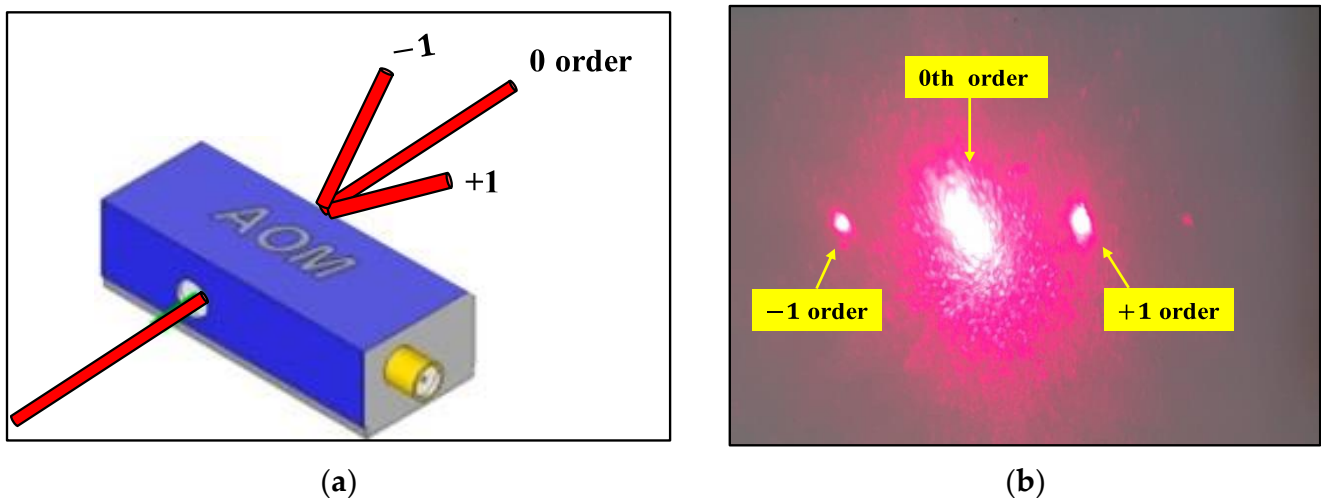

(**a**)   (**b**)

Figure 11. (**a**) Working of AOM; (**b**) observation of higher order modes after modulation of laser from AOM.
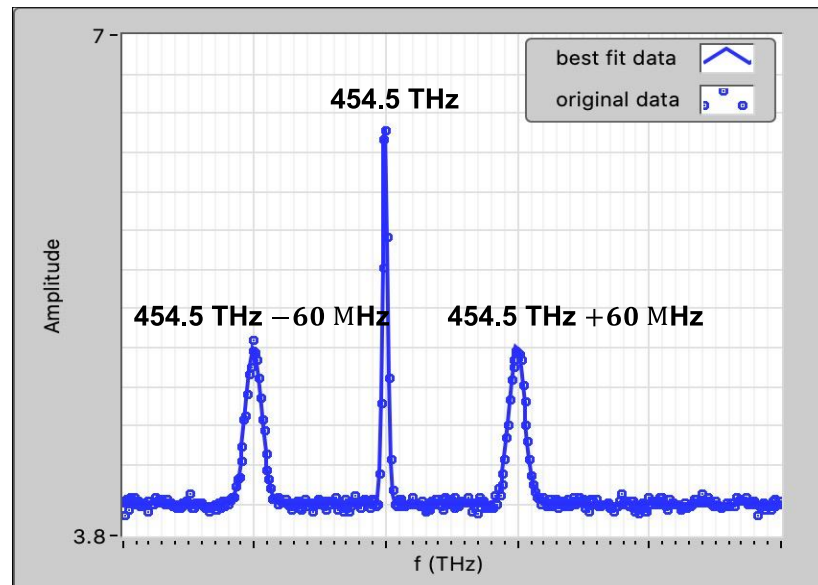
Figure 12. First order modulation of 660 nm laser with AOM with central frequency 60 MHz.

Figure 13a,b shows the optical heterodyne detection setup and measurement of heart frequency at the wrist position of the test subject, respectively. The optical signal is divided into two parts with beam splitter. One part of the optical signal travels in test arm of interferometer which consists of an AOM, while the other part of the optical signal travels in the reference arm of the interferometer. The bio-modulated optical signal reflected from the subject is combined with AOM modulated optical signal at a beam splitter in the test arm. The optical beat signal of test arm and reference arm is obtained at the 3 dB coupler. The measurement procedure on human skin for optical heterodyne detection was the same as that of the optical homodyne detection setup.
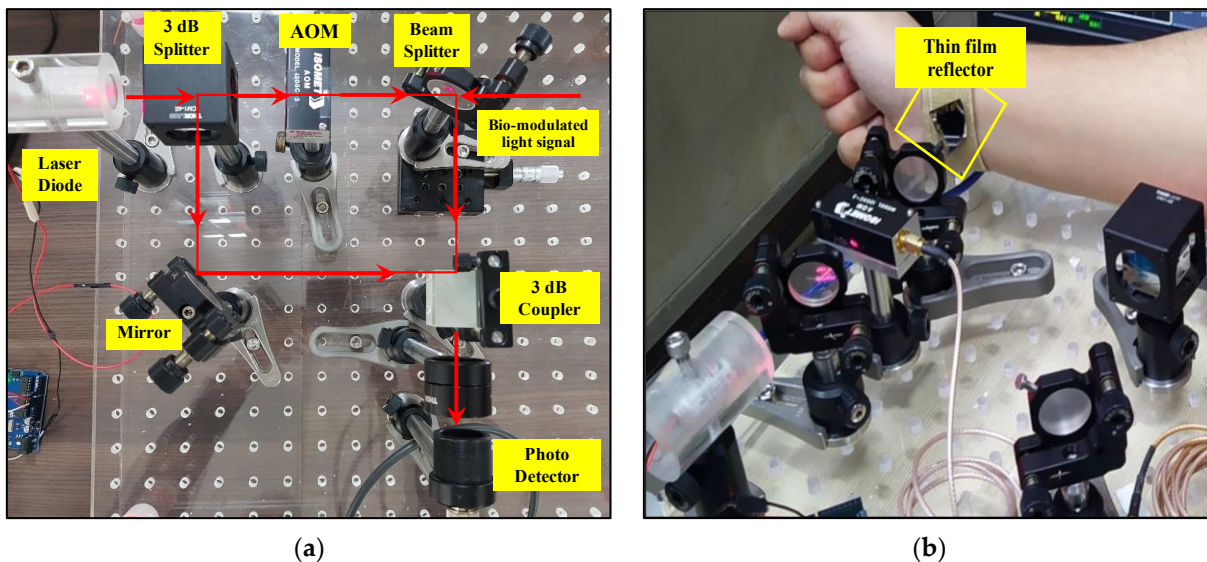

Figure 13. (**a**) Experimental setup for optical heterodyne detection; (**b**) measurement on human wrist position.

Figure 14 shows the response of the photodetector for intermediate frequency f_{IF}. Figure 15 shows the detection of heart frequency f_H. The heart frequency f_H was obtained by demodulation of intermediate frequency f_{IF} with modulation frequency f_m. A frequency mixer was used for the purpose of demodulation and extraction of heart frequency from intermediate frequency.
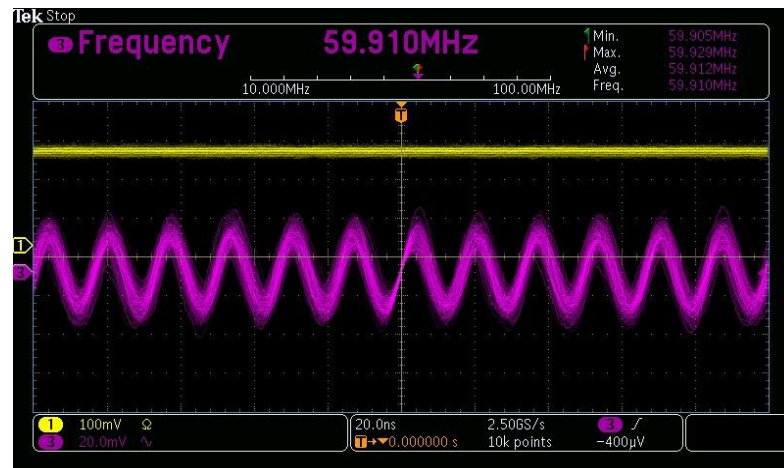
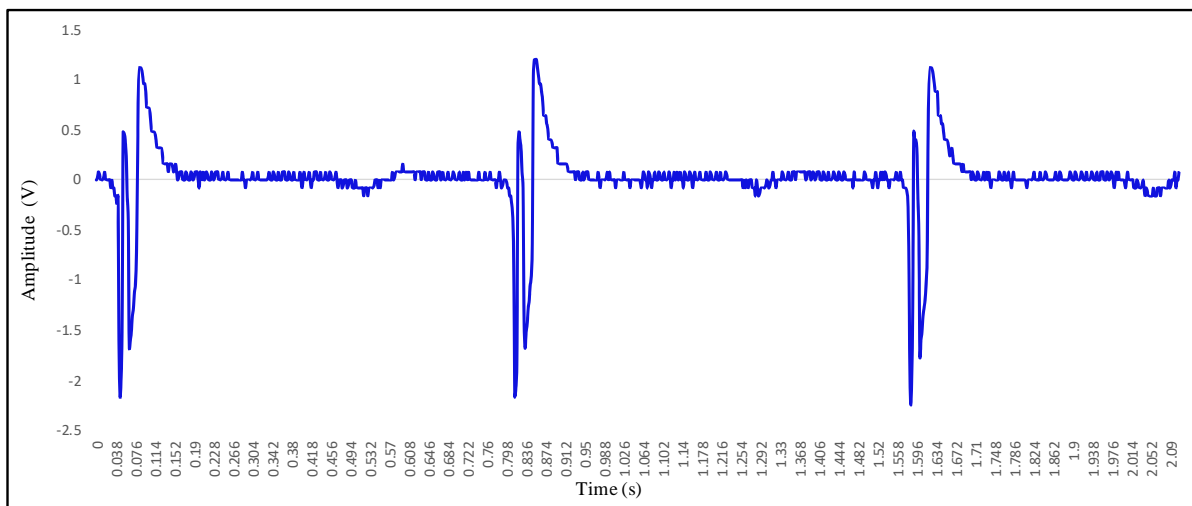**Figure 14.** Modulation frequency along with chest wall frequency detection.

Figure 15. Modulation frequency along with chest wall frequency detection.

4. Measurement Results of *HR* and *HRV* with Optical Homodyne and Heterodyne Technique

HR is measured in average beats per minute, while *HRV* measures the specific changes in time between successive heart beats. A low *HR* indicates rest, while a high *HR* corresponds with physical exertion. The interbeat interval or heart period (HP) is the time between successive heart beats.

4.1. Recording of Vibrocardiogram and Electrocardiogram Signal

It is equally important to compare a non-contact type optical detection method with existing contact type measurement methods, such as ECG. The commercially available AD8232 chip, designed for ultra-low power applications, is used as a contact type sensor for a results comparison with an accuracy of more than 96% [37,38]. AD8232 is used in a three electrode configuration and makes use of right arm (RA), left arm (LA), and right leg (RL) electrodes to acquire bio-potential signal. It has the capability to acquire, amplify, and filter bio-potential signals. This chip is capable of eliminating the motion artifacts and the electrode half-cell potential. The output obtained from the AD8232 module is processed with a microcontroller. The standard PQRST waveform signal is obtained with it. The successive R-R interval (T_{RR}) in milliseconds is calculated for the *HR* measurement. The

detrending and denoising of the raw ECG signal is performed by wavelet analysis. The equation to calculate *HR* in beats per minute is given as,

$$HR = \left(\frac{1}{T_{RR}} \times 60 \right) \tag{24}$$

The optical beat signal obtained from the coherent detection is called a vibrocardiogram (VCG), as the light signal is modulated by vibrations from the chest wall or wrist. On each individual measurement, the ECG and VCG traces were simultaneously recorded. Figures 16–22 shows the detection of the *HR* with optical sensing. Short-term recordings (5 min) were carried out on 20 human subjects (ten males aged from 20 to 40 years; ten females aged from 20 to 40 years). All the participants signed an informed consent agreement before taking part in the tests. The *HR* per minute is measured for a different set of test subjects, with varying physical activities, such as running, walking, speaking, and resting [39]. The ECG and VCG data are recorded for multiple human subjects and are mainly divided into three categories (resting, active, and exertion). Table 3 shows information about the subjects under test.
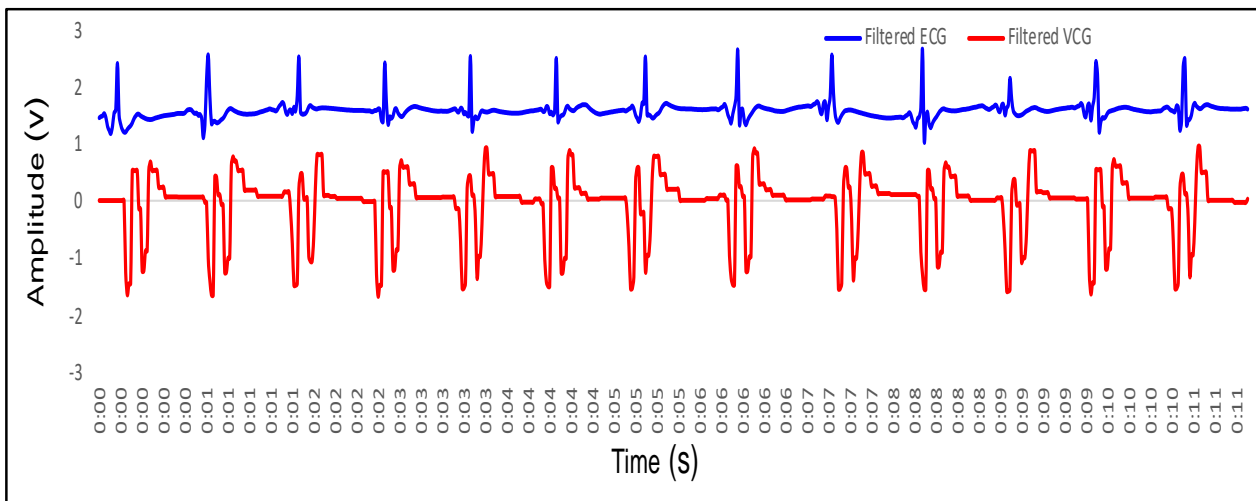

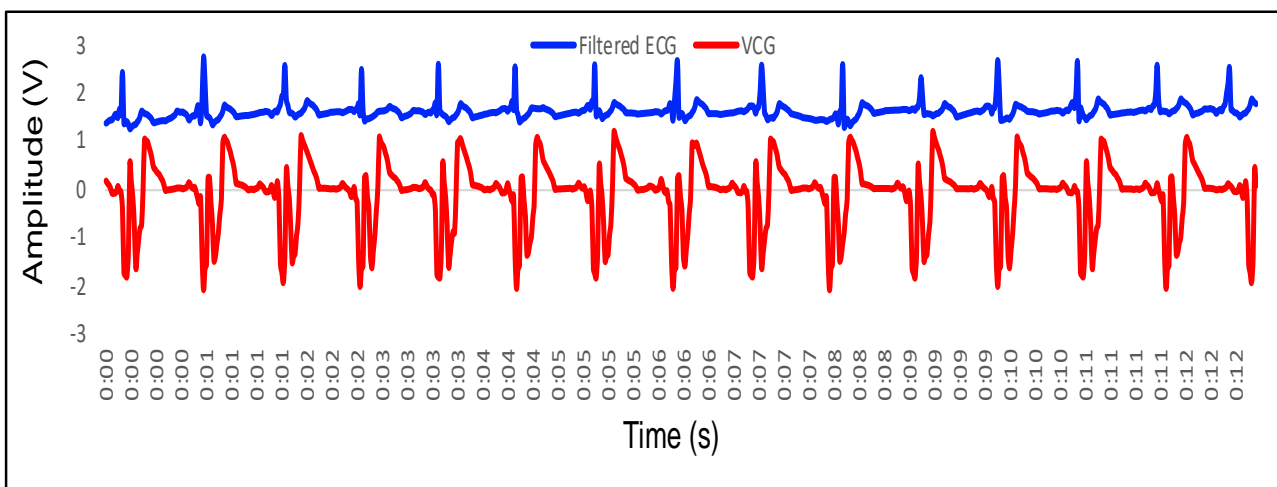**Figure 16.** ECG and VCG signal for 72 heart beats per minute.

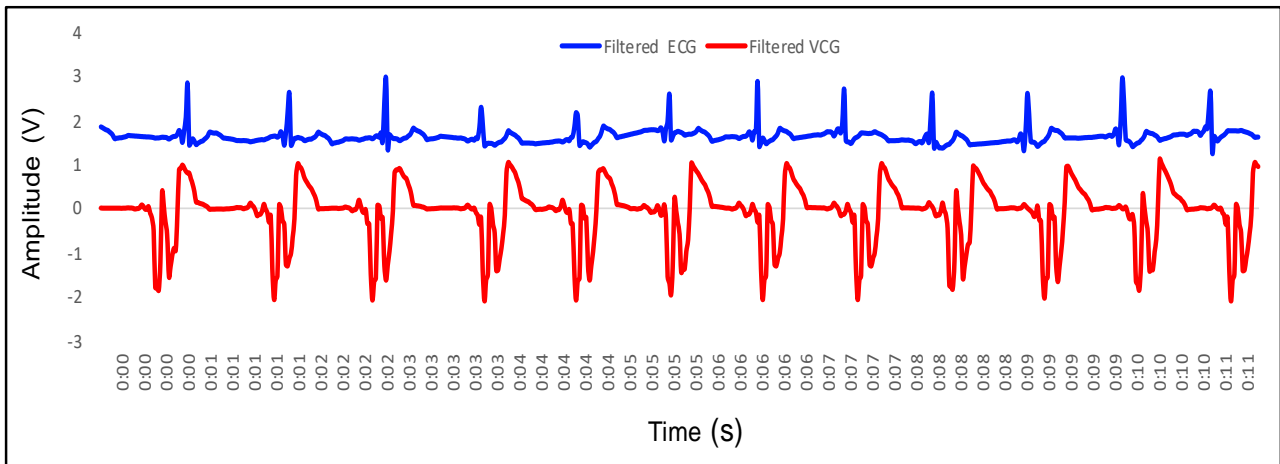**Figure 17.** ECG and VCG signal for 78 heart beats per minute.

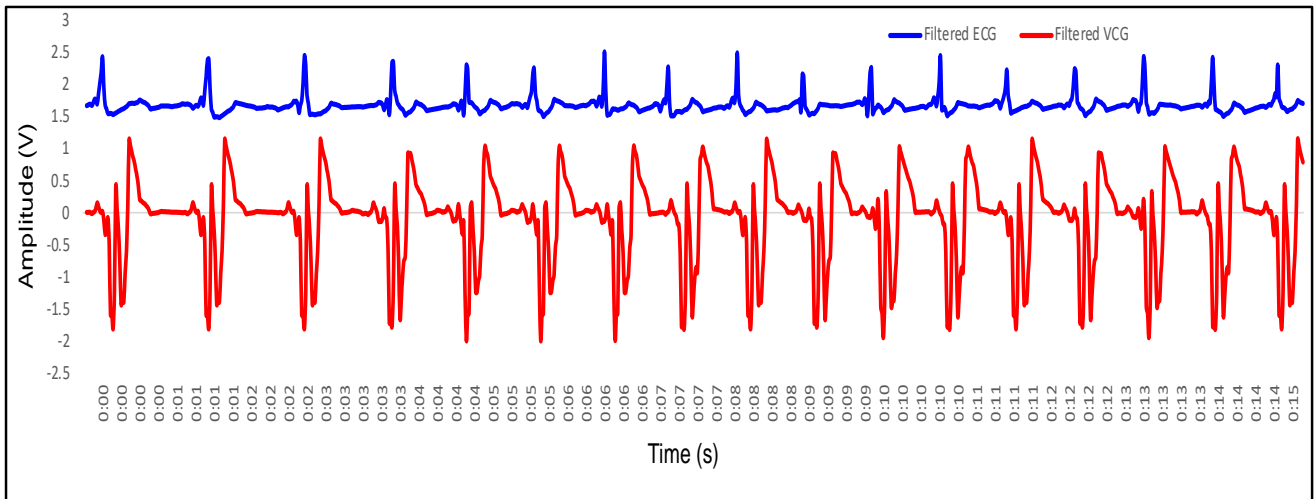**Figure 18.** ECG and VCG signal for 84 heart beats per minute.

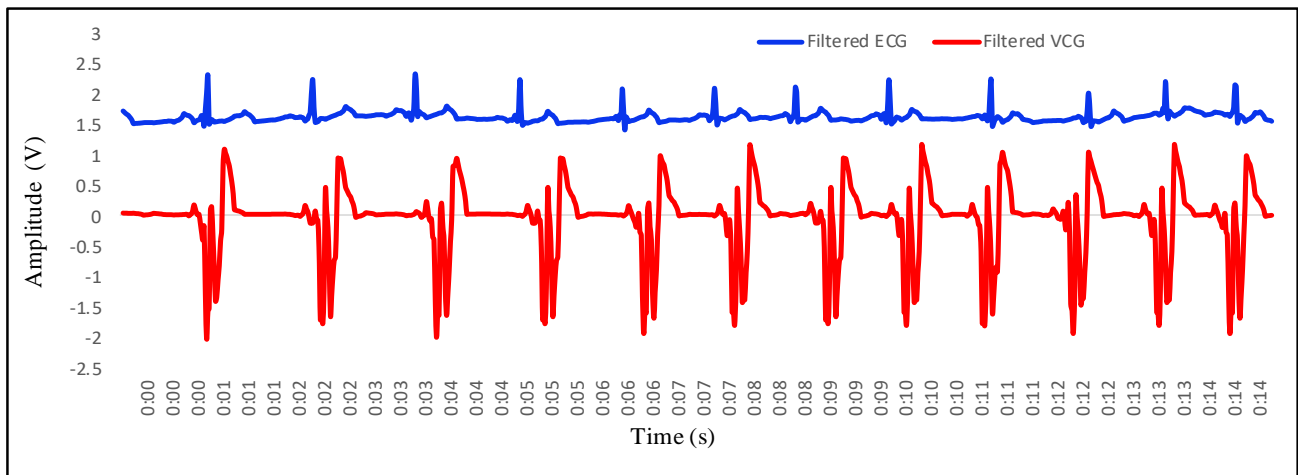**Figure 19.** ECG and VCG signal for 90 heart beats per minute.
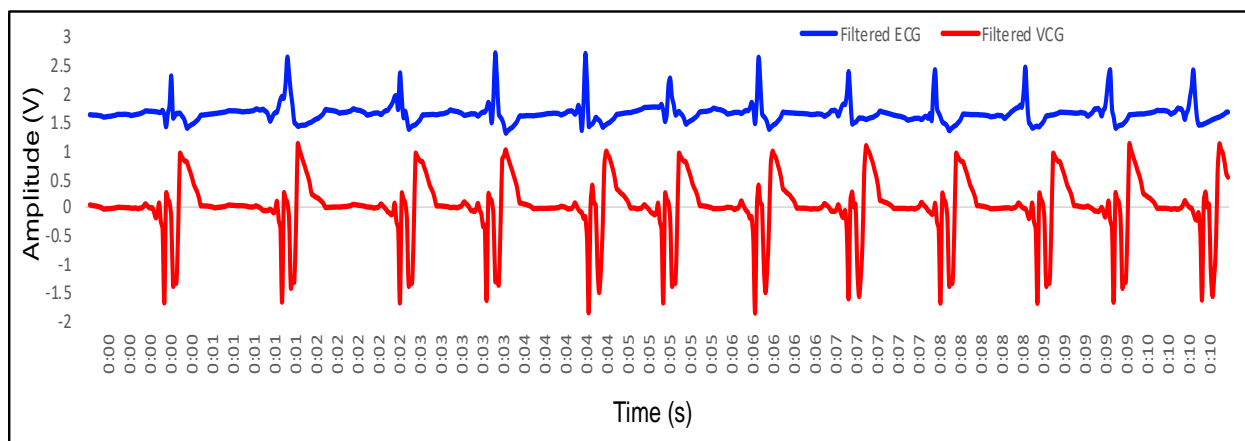

Figure 20. ECG and VCG signal for 96 heart beats per minute.

Figure 21. ECG and VCG signal for 102 heart beats per minute.
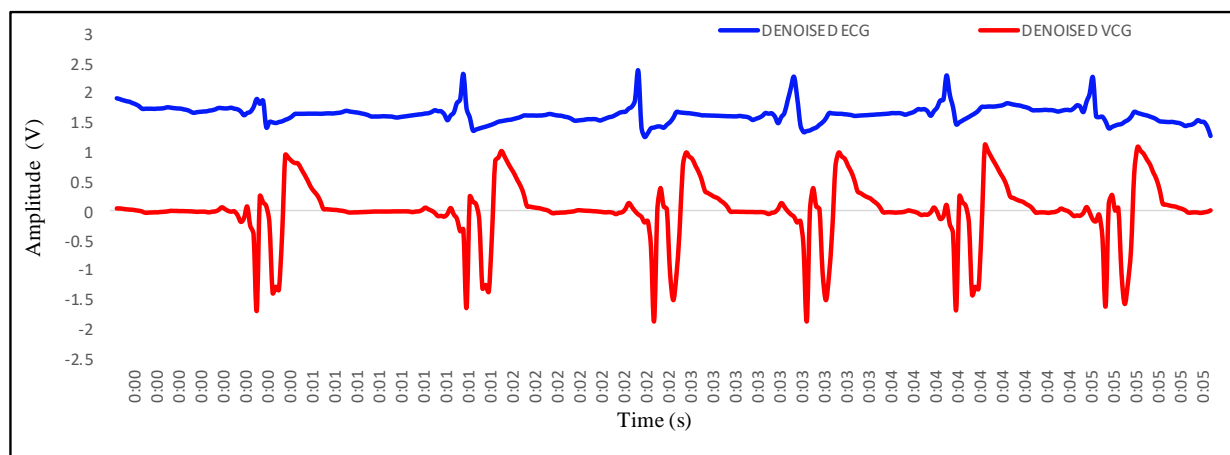
Figure 22. ECG and VCG signal for 108 heart beats per minute.

Table 3. Characteristics of test subjects under test.

Subject Number	Gender	Age (Years)	Weight (kg)	Height (m)	Body Mass Index (BMI) (kg·m^{-2})
1	M	20	61	1.71	20.86
2	M	20	59	1.69	20.65
3	M	22	64	1.73	21.38
4	M	22	66	1.75	21.55
5	M	25	68	1.79	21.22
6	M	25	64	1.75	20.89
7	M	30	65	1.70	22.49
8	M	32	67	1.84	19.78
9	M	38	69	1.77	22.02
10	M	40	70	1.76	22.59
11	F	20	55	1.76	17.75
12	F	20	53	1.71	18.12
13	F	22	57	1.74	18.82
14	F	25	64	1.78	20.20
15	F	25	58	1.73	19.37
16	F	28	68	1.80	20.98
17	F	30	64	1.78	20.19
18	F	32	63	1.70	21.79
19	F	38	67	1.75	21.87
20	F	40	69	1.65	25.34

For the *HR* measurement of physical exertion, the test subjects were asked to go through excessive physical activities, such as climbing stairs or exercise, just before the measurement. Physical exertion leads to artifacts in the measurement on the test subject. These artifacts are basically associated with a high respiration rate, which causes rapid change in the chest wall motion. Frequent motion of the chest wall leads to shift in the baseline of the VCG signal. The motion artifacts associated with respiration are always present in the *HR* signal in the form of baseline wandering. The baseline drift is removed by denoising and detrending. Figure 23 shows the VCG signal for 72 bpm, 90 bpm, and 102 bpm with the same time axis. From Figure 23, the VCG signals with different *HR* can be identified easily.
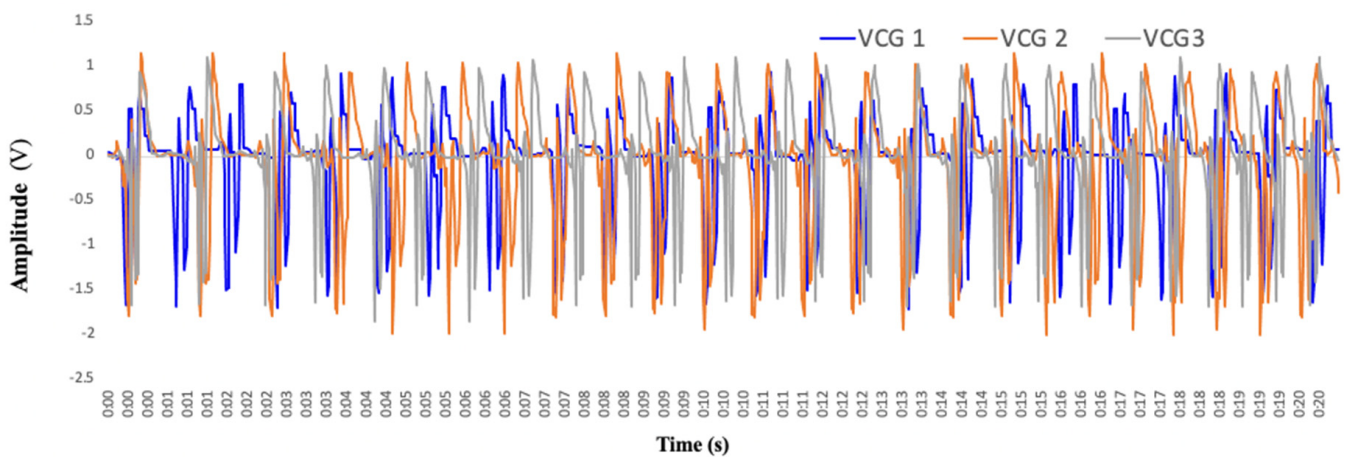

Figure 23. VCG signals obtained for different values of *HR*: VCG1, 72 bpm; VCG2, 90 bpm; VCG3, 102 bpm.

4.2. Feature Extraction in VCG and Its Mapping with ECG

The oxygen-rich blood returns from the lungs and flows into the heart's upper left atrium. The oxygen-depleted blood returns from the rest of the body and flows into the right atrium. Both the left and the right atria become filled with blood. The sinus node (SA) in the right atrium produces a small electrical pulse. The systole and diastole are the two processes that are associated with the period of contraction and relaxation of the heart, respectively. The electrical pulse causes the heart contraction. Due to this, mechanical vibrations are originated and propagate through different tissue layers before being detected on the skin with an optical sensing technique [40]. The factors which influence the vibration signal are the time and amplitude characteristics of the electrical pulse and the mechanical response of the heart. These factors depend on specific characteristics, such as body mass index (BMI) and the medical history for the disease. It is important to map the electrical activity of the heart with its mechanical response, as it provides useful information about the activity of the heart. In the following section, the mapping of ECG and VCG is performed, and its significance is explained.

1. P wave: The P wave represents the depolarization of the left and right atrium. It corresponds to atrial contraction. The point of local maximum in the ECG for the P wave corresponds to the point of the first local minima U_1 in the VCG, as shown in Figure 24. The opposite nature of the electrical and mechanical signal is due to atrial contractions [41];
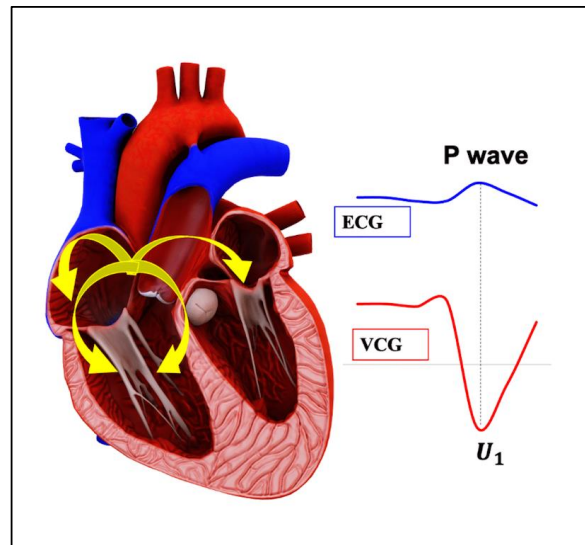
Figure 24. Mapping of P wave of ECG and U_1 wave of VCG.

2. PR interval: During the PR interval, the electrical pulse moves from atria to ventricles. The PR interval in the ECG has a duration of approximately 120–200 ms. The contractions of ventricles generate vibration patterns that are observable in the VCG plot. When the ventricle contracts, a dominant negative deflection is generated. Thus, it is possible to distinguish between a heartbeat and a beat drop. The atrial contractions result in positive deflections. The PR interval in the ECG is mapped to the interval between the first local minima U_1 and the second zero crossing of the VCG signal;

3. QRS complex: The point Q in the ECG corresponds to the point of first local maximum V_1, while the point of minimum S in the ECG corresponds to the point of second local minima U_2 in the vibrocardiogram signal, as shown in Figure 25. The R wave in the ECG corresponds to the zero crossing of the VCG signal [42]. The zero crossing is a point which is located at the center of V_1 and U_2. It is located exactly at the center of the first maxima and the second minima of the VCG signal.
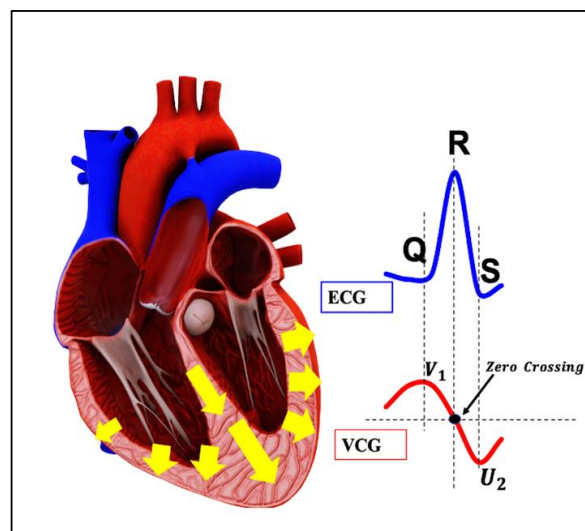

Figure 25. Mapping of QRS complex of ECG and V_1U_2 complex of VCG.

The total time duration of the QRS signal represents the depolarization of ventricles. During this time interval, the chest wall vibration reduces significantly from maximum to minimum;

4. ST segment: The T wave represents ventricular repolarization. It appears as a small wave after the QRS complex. The ST segment starts at the end of the S wave and ends at the beginning of the T wave. The ST segment is an isoelectric line that represents the time between depolarization and repolarization of the ventricles. The T wave in the ECG corresponds to the V_2 wave of the VCG, as shown in Figure 26;
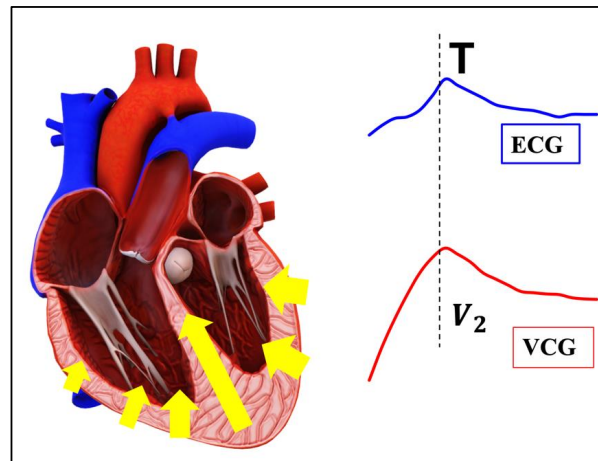

Figure 26. Mapping of T wave of ECG and V_2 wave of VCG.

5. QT interval: The QT interval begins at the start of the QRS complex and finishes at the end of the T wave. The QT interval in the ECG is mapped to the V_1V_2 interval of the VCG. It represents the time taken for the ventricles to depolarize and then repolarize [43].

The complete VCG cycle is mapped to the ECG cycle for the heart period (HP). Figure 27 shows the significance of features in the VCG with reference to the ECG. From the recordings of both the signals, the relationship between the ECG to the vibratory signal VCG in terms of heart rate variations is analyzed. The peak vibratory signal is due to chest wall motion. This signal is generated due to cardiac muscle contraction triggered by the electrical signal. The first local maximum value is labeled as V_1 in the VCG, while the first local maximum in the ECG curve is labeled as R. For the measurement of HR and HRV, V-V interval (T_{VV}) is considered, and this measurement is compared with the R-R interval (T_{RR}) in the ECG trace [44]. By using Equation (23), the HR can be calculated from the VCG signal as,

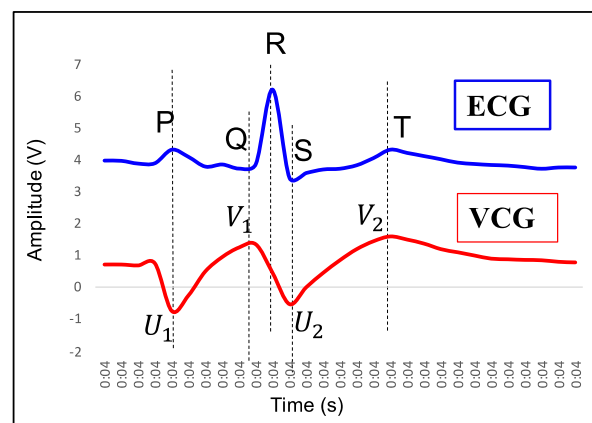$$HR = \left(\frac{1}{T_{VV}} \times 60 \right)$$ (25)

Figure 27. Mapping of complete ECG wave with VCG wave.

4.3. Measurement of HRV

The time difference between two successive R peaks is calculated throughout the ECG wave. The mean value of this time difference is called the R period. Similarly, the time difference between two successive V_1 peaks is calculated, and this time difference is called the V period. The R period and V period provide the time duration for each heart activity. The difference between two consecutive R period intervals is calculated as the R-R variability, while the difference between two consecutive V period intervals is calculated as the V-V variability [45]. In this experiment, different subjects with different ages and BMI are considered. Table 4 shows an example of the measurement of the heart period and *HRV* by means of ECG and VCG waveforms. For this measurement, the test subject was in a state of rest. In order to measure the *HRV*, the periodic characteristic related to the heartbeat needs to be identified [46].

Table 4. Heart period and *HRV* measurement for test subject under relax condition with ECG and VCG analysis.

Heartbeat Count	R Period (s)	R-R Variability (s)	U Period (s)	V Period (s)	V-V Variability (s)
1	0.256836	-	0.23564	0.27564	-
2	1.283203	1.026367	1.207031	1.247031	0.971391
3	2.301758	1.018555	2.2177735	2.2577735	1.0107425
4	3.321289	1.019531	3.2285155	3.2685155	1.010742
5	4.28125	0.959961	4.25	4.29	1.0214845
6	5.303711	1.022461	5.2714845	5.3114845	1.0214845
7	6.291992	0.988281	6.2929685	6.3329685	1.021484
8	7.303711	1.011719	7.314453	7.354453	1.0214845
9	8.256836	0.953125	8.324453	8.364453	1.01
10	9.303711	1.046875	9.364453	9.404453	1.04
11	10.2978515	0.9941405	10.324453	10.364453	0.96
12	11.3427735	1.044922	11.2914453	11.3314453	0.9669923
13	12.2714845	0.928711	12.3214453	12.3614453	1.03
14	13.276367	1.0048825	13.314453	13.354453	0.9930077
15	14.256836	0.980469	14.314453	14.354453	1
16	15.321289	1.064453	15.3231445	15.3631445	1.00869153
17	16.41289	1.091601	16.354453	16.394453	1.03130847
18	17.361289	0.948399	17.384453	17.424453	1.03
19	18.381289	1.02	18.384453	18.424453	1
20	19.5289	1.147611	19.434453	19.474453	1.05

From Table 4, the mean value of the R-R interval is calculated to be 101.056 ms with a standard deviation of 48.8 ms and a standard error value of 6 ms, while the mean value of the V-V interval is calculated to be 101.257 ms with a standard deviation of 36.3 ms and a standard error of 4 ms. The UU variability and VV variability are equal, as they are part of the same signal. Therefore, for further analysis of *HRV*, only one of UU or VV variability is considered.

Figure 28 shows the column chart representation of variability in the R-R interval, U-U interval, and V-V interval, simultaneously. The heart period for each heartbeat count for both the ECG and VCG signal is represented as a vertical column line. For the VCG signal, the heart interval is measured for both the U-U and V-V wave, while the R-R wave is considered for the ECG [47]. From Figure 26, it is clear that the measurement of *HRV* from the ECG and VCG plots shows similar results, with a less than 1% deviation value. Figures 29 and 30 show the R-R and V-V variability plot for the test subject under sleep. A *HR* of 40 bpm is measured with the test subject under deep sleep. Figure 31 shows *HRV* analysis of the test subject under an active state, and a *HR* of 72 bpm is measured. Figures 32 and 33 show *HRV* analysis of the test subject under excessive stress and physical exertion, respectively. A *HR* of 96 bpm and 108 bpm are recorded for test subjects under excessive stress and physical exertion, respectively. All results shown here are obtained on the chest wall. Figure 34 shows the *HRV* in the ECG and VCG for different test subjects. The

measurement of *HRV* from the VCG shows much less deviation from their corresponding ECG values.

Figure 28. Comparison of R-R, U-U, and V-V variability from ECG and VCG for *HR* 60 bpm.

Figure 29. Comparison of R-R and V-V variability from ECG and VCG for test subject under sleep.

Figure 30. Comparison of R-R and V-V variability from ECG and VCG for *HR* 54 bpm.

Figure 31. Comparison of R-R and V-V variability from ECG and VCG for *HR* 72 bpm.
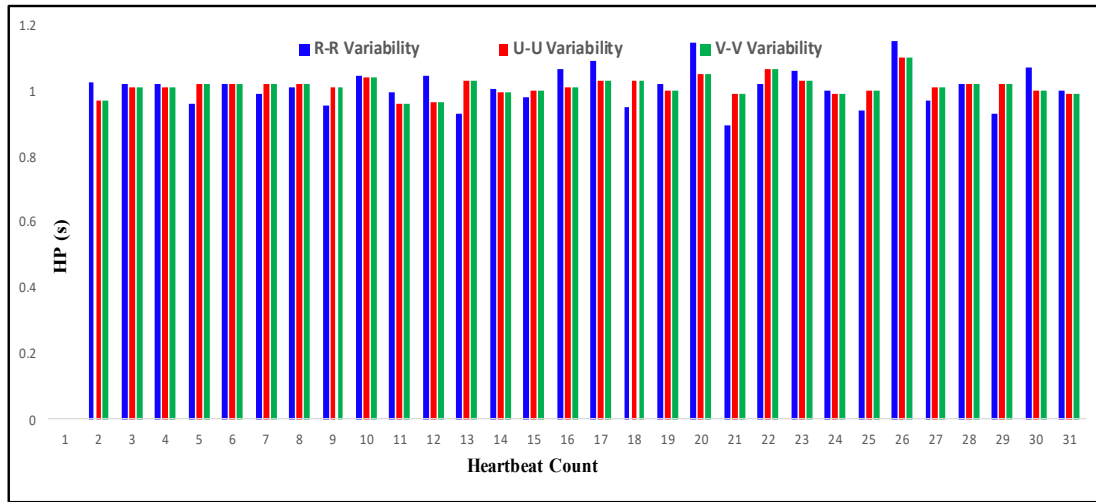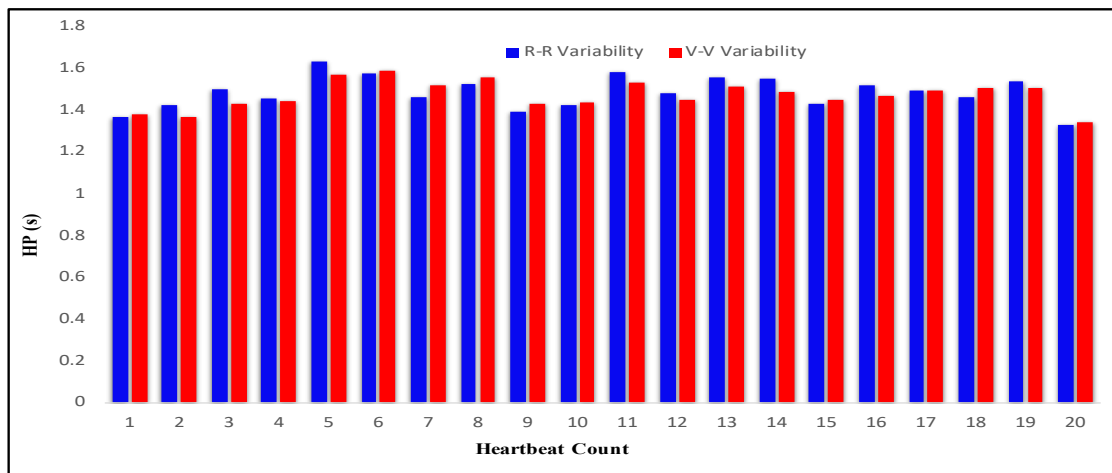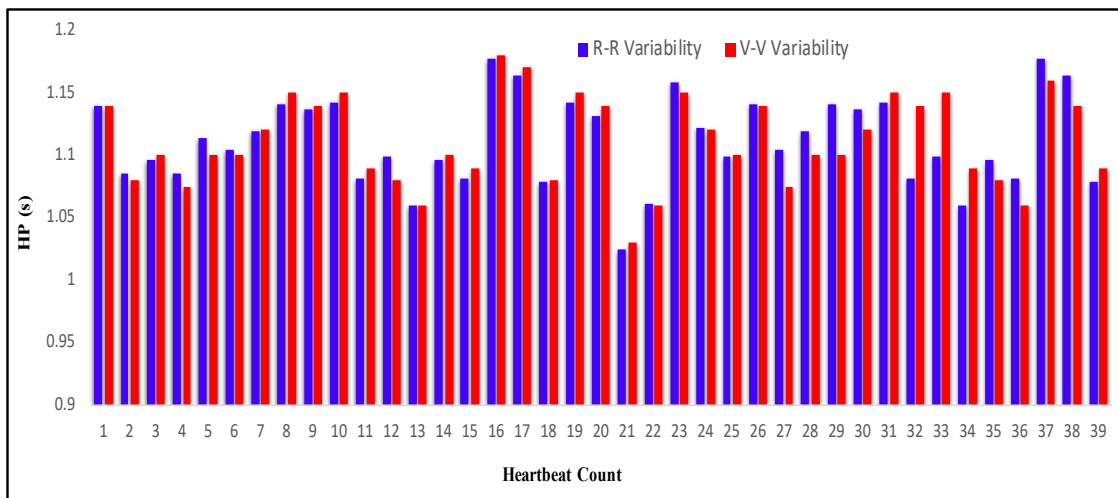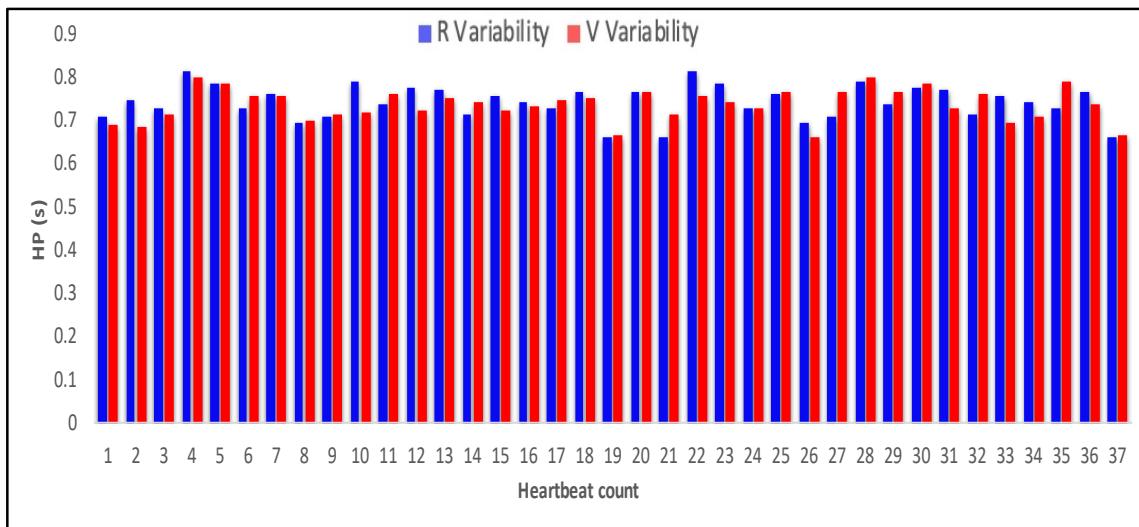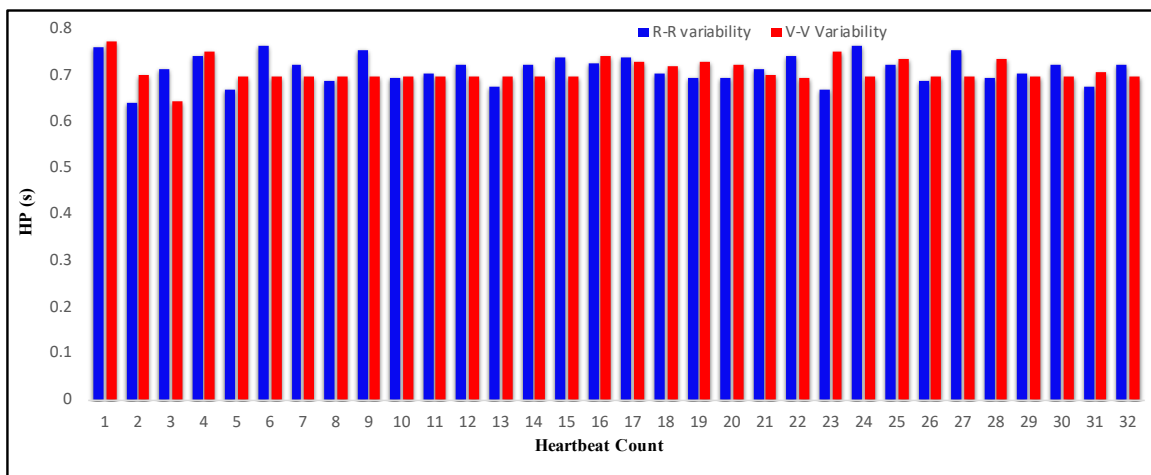

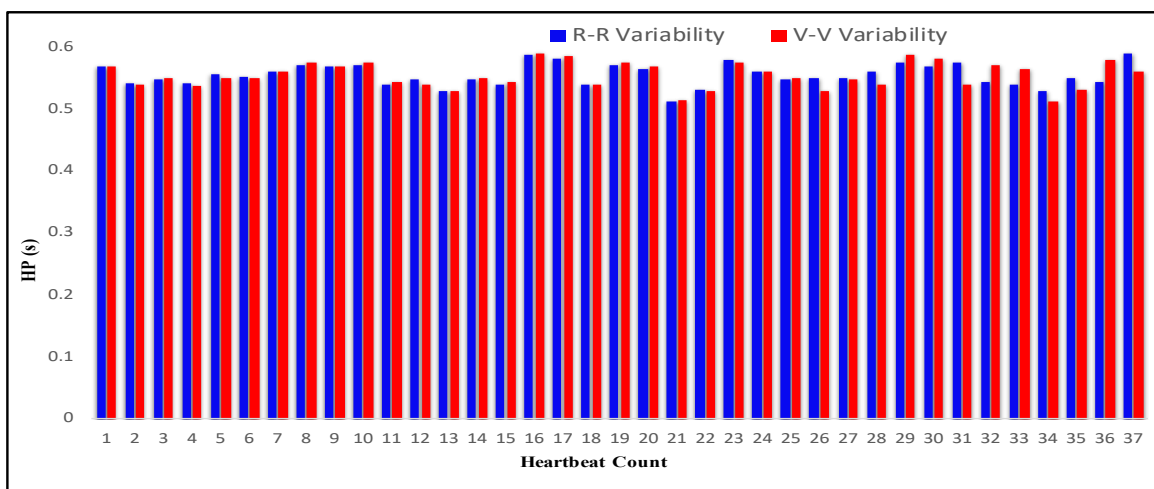**Figure 32.** Comparison of R-R and V-V variability from ECG and VCG for *HR* 96 bpm.

Figure 33. Comparison of R-R and V-V variability from ECG and VCG for *HR* 108 bpm.
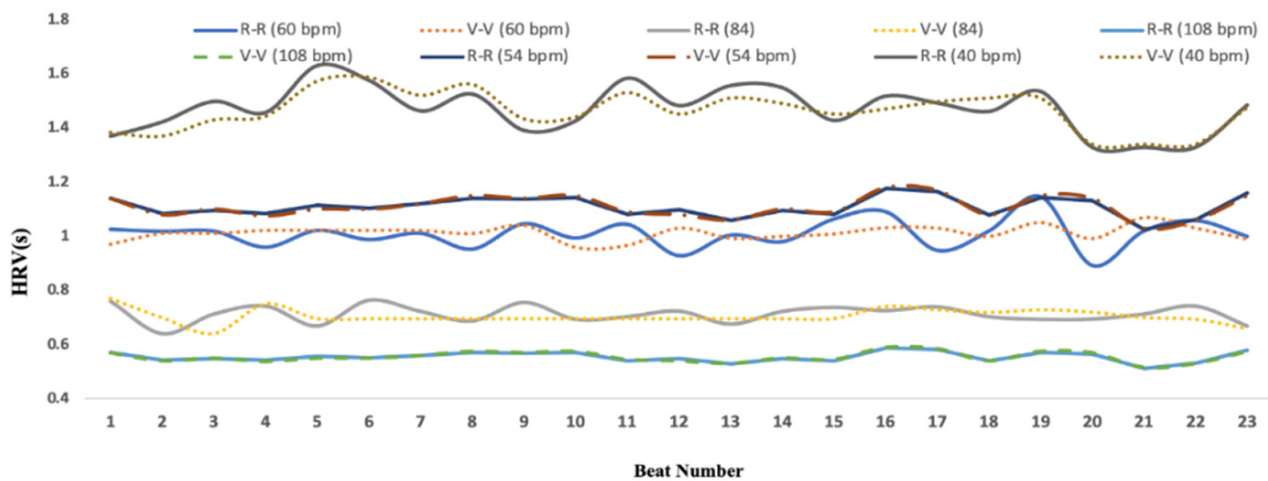
Figure 34. R-R and V-V variability from ECG and VCG for different values of *HR*.

Table 5 shows a complete summary of *HR* and *HRV* for different test subjects under deep sleep, active state, and excessive exertion. It is clear that the ECG recording and VCG recording show similar results for *HRV* and *HR*. For non-contact type measurement, both homodyne and heterodyne detection techniques are used. The *HR* and *HRV* values obtained from homodyne and heterodyne detection show much less deviation from the ECG values.

Table 5. Analysis of variability from RR and VV interval (measurement on chest wall).

Subject No.	R-R Variability ECG (ms)	V-V Variability Heterodyne (ms)	V-V Variability Homodyne (ms)	*HR* in bpm (ECG)	*HR* in bpm (Heterodyne)	*HR* in bpm (Homodyne)
1	555 ± 3	554.5 ± 3	554 ± 3	108.02	108.20	108.30
15	713 ± 5	711 ± 3	709 ± 5	84.13	84.38	84.60
12	745 ± 6	742 ± 3	741 ± 6	80.54	80.86	80.97
16	854 ± 8	852 ± 4	849 ± 5	70.26	70.42	70.67
5	1010 ± 6	1012 ± 4	1012 ± 4	59.37	59.29	59.25
7	1112 ± 6	1111 ± 6	1111 ± 6	53.96	54.00	54.00
19	1431 ± 10	1430 ± 8	1429 ± 8	41.92	41.96	42.00
10	1484 ± 17	1482 ± 8	1480 ± 15	40.41	40.54	40.68

4.4. Comparison of Results of Optical Homodyne and Heterodyne Technique

The accuracy of heterodyne detection is found to be better than homodyne detection. The use of AOM in heterodyne detection limits the noise associated with the laser oscillator. However, both optical coherent detection techniques show much less deviation from the ECG recording. Table 6 shows a comparison of results obtained from homodyne detection and heterodyne detection and their deviation from the ECG results. The mean deviation between the electrical measurement and optical measurement methods for each subject is reported [48–50] and computed with the equation,

$$Deviation = HR_{VCG} - HR_{ECG} \qquad (26)$$

A small value of deviation from the ECG proves that the VCG graph provides an accurate measurement of *HR* and *HRV*. As shown in Table 6, the deviation values between the VCG and ECG approaches zero for a measurement of *HR* lower than 70 bpm. For a measurement of *HR* higher than 70 bpm, the deviation values are less than 0.5. The measurement of higher *HR* is associated with many factors, such as medical history and the psychological and emotional behavior of the subject under test.

Table 6 clearly shows that *HR* values obtained from both techniques are very close to *HR* values obtained from the ECG recording. The obtained results are motivating because

optical detection is a completely non-contact type measurement technique. Table 7 shows the values of *HR* obtained from the coronary artery (chest wall position) and radial artery (wrist position) of two test subjects. The measurement of *HR* at the coronary artery and radial artery shows very little deviation, at less than 1 bpm.

Table 6. Deviation in *HR* for optical homodyne and heterodyne detection.

Subject Number	*HR* in bpm (ECG)	*HR* in bpm (Heterodyne)	*HR* in bpm (Homodyne)	Deviation in bpm (Heterodyne)	Deviation in bpm (Homodyne)
1	108.02	108.2	108.3	0.18	0.28
15	84.13	84.38	84.6	0.25	0.47
12	80.54	80.86	80.97	0.32	0.43
16	70.26	70.42	70.67	0.16	0.41
5	59.37	59.29	59.25	−0.08	−0.12
7	53.96	54	54	0.04	0.04
19	41.92	41.96	42	0.04	0.08
10	40.41	40.49	40.54	0.08	0.13

Table 7. Deviation in *HR* for optical homodyne and heterodyne detection.

Subject No.	Measurement Site	*HR* in bpm (Homodyne)	*HR* in bpm (Heterodyne)
5	Coronary Artery	59.29	59.25
5	Radial Artery	60.12	60.04
15	Coronary Artery	84.38	84.6
15	Radial Artery	85.22	84.9

Figure 35a,b shows a comparison of homodyne and heterodyne techniques for the measurement of a *HR* of 54 bpm and 84 bpm, respectively. It is clear from Figure 35a that homodyne and heterodyne detection show identical results for measurement associated with the lower value of *HR*. Figure 36b shows a deviation of 0.22 bpm when measuring the higher value of *HR*. The measurement of deviation of the VCG values from ECG values are performed for both homodyne and heterodyne techniques. Figure 36a,b shows the mapping of the heterodyne and homodyne signal with the ECG signal for a *HR* of more than 70 bpm, respectively. Figure 36a shows that the R peak of the ECG precisely maps to the zero crossing between the V_1 point and U_2 point in the VCG associated with the heterodyne measurement system. Figure 36b shows that there is a small delay Δt between the R peak of the ECG and the zero crossing between the V_1 point and U_2 point in the VCG associated with the homodyne measurement system. These results show that for measurement of a higher value of *HR*, optical heterodyne measurement provides better accuracy compared to optical homodyne measurement. The delay Δt approaches to zero for the heterodyne measurement system. However, the delay Δt measured for homodyne detection is found to be less than 3 ms. The delay Δt leads to a maximum deviation of around 0.5 bpm from the ECG values. Thus, measurements recorded with the optical homodyne setup are comparable with both the optical heterodyne and ECG setup. The deviation values from the ECG are found to be less than 1%. Figure 37 shows the deviation of both techniques from the ECG values. Figure 38a,b shows the distribution of the deviations in bpm for the case of chest wall measurement (subject 7). The histogram is fitted with a Gaussian distribution, with a mean value of 0.04 bpm and a standard deviation of 1.1 bpm for heterodyne detection. The histogram is fitted with a Gaussian distribution mean value of 0.06 bpm and a standard deviation of 1.6 bpm for homodyne detection. The value of uncertainty calculated with the heterodyne detection method is ±0.14 bpm, while for the homodyne detection method, the value of uncertainty is calculated as ±0.25 bpm.
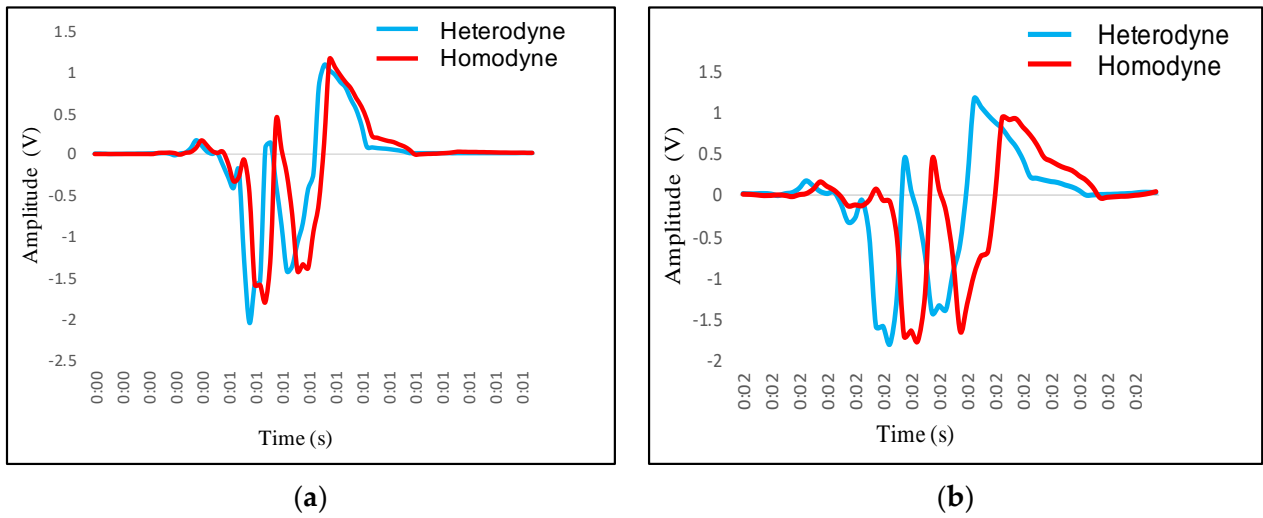
Figure 35. (**a**) Mapping of homodyne and heterodyne VCG trace for measurement of *HR* 54 bpm; (**b**) mapping of homodyne and heterodyne VCG trace for measurement of *HR* 84 bpm.
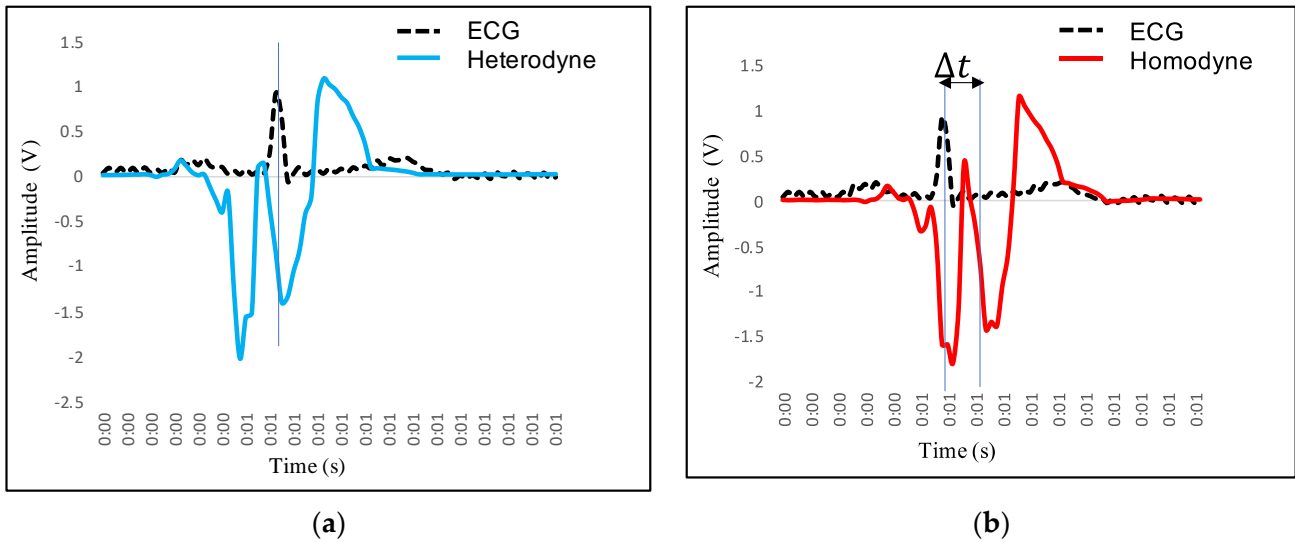

Figure 36. (**a**) Mapping of optical heterodyne VCG trace with ECG for measurement of *HR* more than 70 bpm; (**b**) mapping of optical homodyne VCG trace with ECG for measurement of *HR* more than 70 bpm.
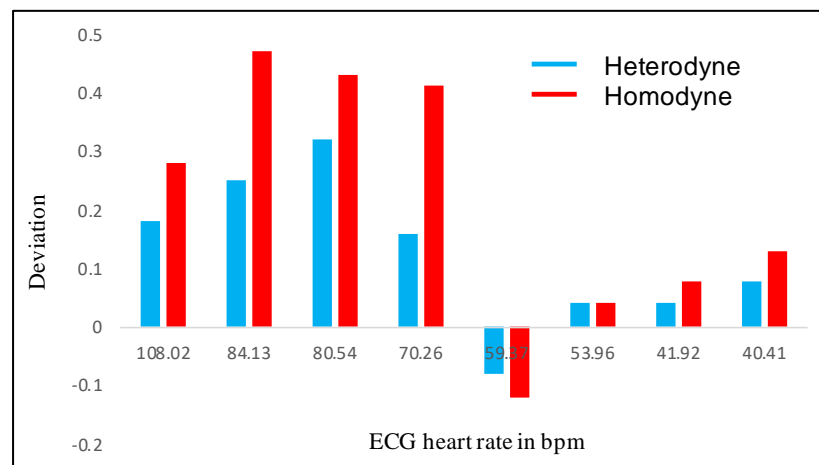

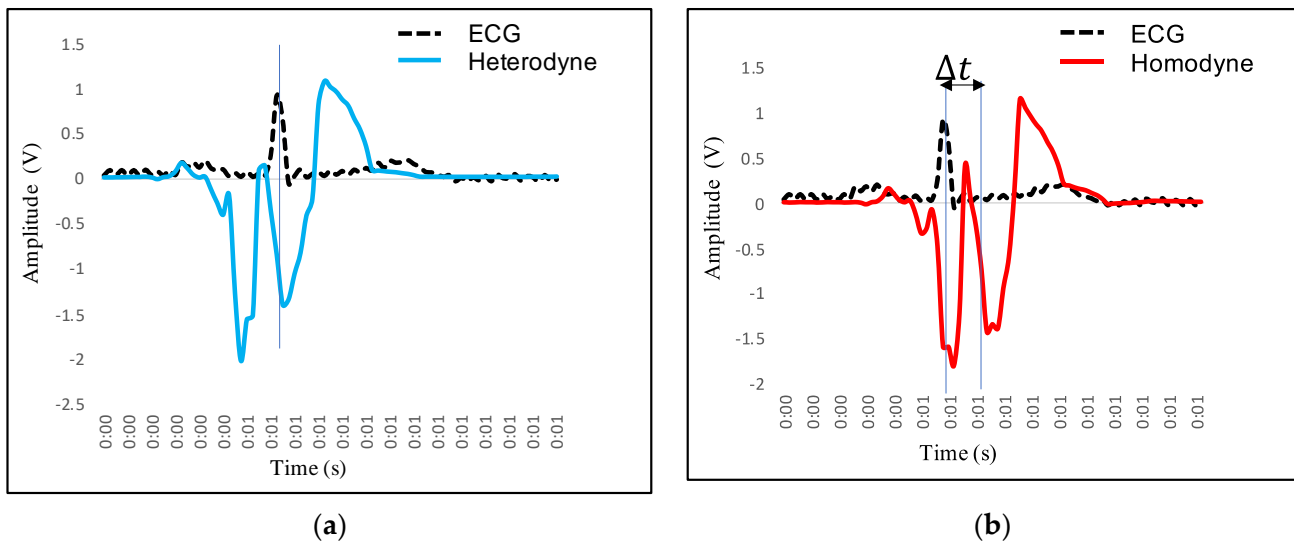**Figure 37.** Deviation of heterodyne and homodyne measurement from ECG.

Figure 38. (**a**) Deviations of *HR* measured with heterodyne system with respect to ECG (chest wall measurement, subject 7); (**b**) deviations of *HR* measured with homodyne system with respect to ECG (chest wall measurement, subject 7).

5. Discussion

Self-mixing optical coherent detection is an important sensing method for the assessment of cardiac, respiratory, and muscular activities. *HRV* is an important parameter to analyze both the overall health and the ability to tolerate stress [51]. Optical coherent detection techniques have the advantage of being a contactless method, as it becomes very helpful in measurements from critically damaged skin conditions. They are also useful for measurements on the delicate skin of preterm infants. HP can be measured by detecting a periodic feature in the waveform acquired, such as V_1 and V_2 peaks in the VCG signal. A comparison of R peaks in the ECG with V peaks in the VCG signal was performed and both the measurements were found to be similar, with a less than 1% deviation. The mapping of features of the ECG signal is performed with VCG signal features [52]. In this research paper, measurement results from homodyne and heterodyne techniques are compared with the ECG signal. In future, the accuracy of homodyne and heterodyne measurements can be compared with other signals of a different nature, such as the photoplethysmograph (PPG) and phonocardiogram (PCG). The ECG is the electrical signal, which is a representation of the electrical response of the heart activity. The PCG is the audio signal and represents the acoustic response of the heart activity. The PPG is the optical signal, while the VCG is the mechanical signal. During an arrhythmia, the heart can beat too fast, too slowly, or with an irregular rhythm. The first-degree AV block occurs when the PR interval is more than 200 ms. The AV block can be easily correlated with the VCG signal when there is a delay between U_1 and the zero crossing of the VCG signal [53]. The stability of coherent detection can be improved by the construction of a multiple mirror Fabry–Perot resonator in one of the arms of the interferometer, or by implementing a servo motor mechanism for the motion of mirrors [54–58].

6. Conclusions

In this research, a novel design of optical homodyne and optical heterodyne detection is explained. The optical homodyne technique consists of a simple setup, but the optical heterodyne technique makes use of complex optical components, such as AOM. The optical homodyne detection makes use of the direct modulation of the fundamental optical signal, while the optical heterodyne detection technique makes use of the modulation of the higher order mode of the optical signal. The path length fluctuations are the main problem in optical homodyne detection. The phase fluctuations related to the path length difference can have very little variation in a homodyne setup. This problem can be solved with optical heterodyne detection, as the frequency of the local oscillator is not equal to the

signal frequency in optical heterodyne detection ($f_s \neq f_{LO}$). In case of measurement of high values of *HR* (more than 70 bpm), the optical heterodyne detection has a higher accuracy of results compared to optical homodyne detection. This is due to the fact that variation in the path length difference is very limited in the homodyne setup ($\Delta L \leq \frac{\lambda}{4}$). However, results obtained from the homodyne method show much less deviation from results of the heterodyne setup and ECG setup. The deviation of results is less than 3 ms for measurement of the heart period and less than 0.5 bpm for measurement of the *HR*. Both homodyne and heterodyne detection techniques can be used to accurately measure *HR* and *HRV*. The experimental results of homodyne and heterodyne detection are comparable with contact type measurement methods, such as an ECG. The results are found to be within a less than 1% deviation value from the ECG measurement.

Author Contributions: J.G. performed the conceptualization, methodology, software, validation, formal analysis, and investigation. M.S.P. performed the supervision and project administration. The writing, review, editing, and visualization are carried out by J.G. All authors have read and agreed to the published version of the manuscript.

Informed Consent Statement: Informed consent was obtained from all subjects involved in the study.

Data Availability Statement: The data presented in this study are available on request from the corresponding author. The data are not publicly available due to privacy issues.

Conflicts of Interest: The authors declare no conflict of interest.

References

1. Tanzi, L.; Vezzetti, E.; Moreno, R.; Aprato, A.; Audisio, A.; Massè, A. Hierarchical fracture classification of proximal femur X-Ray images using a multi-stage deep learning approach. *Eur. J. Radiol.* **2020**, *133*, 109373. [CrossRef]
2. El-Saadawy, H.; Tantawi, M.; Shedeed, H.A.; Tolba, M.F. *Deep Learning Method for Bone Abnormality Detection Using Multi-View X-rays, International Conference on Artificial Intelligence and Computer Vision*; Springer: Cham, Switzerland, 2021; pp. 46–55.
3. Schroeder, E.B.; Liao, D.; Chambless, L.E.; Prineas, R.J.; Evans, G.W.; Heiss, G. Hypertension, Blood Pressure, and Heart Rate Variability. *Hypertension* **2003**, *42*, 1106–1111. [CrossRef] [PubMed]
4. Mejía-Mejía, E.; Budidha, K.; Abay, T.Y.; May, J.M.; Kyriacou, P.A. Heart Rate Variability (HRV) and Pulse Rate Variability (PRV) for the Assessment of Autonomic Responses. *Front. Physiol.* **2020**, *11*, 779. [CrossRef] [PubMed]
5. Sessa, F.; Anna, V.; Messina, G.; Cibelli, G.; Monda, V.; Marsala, G.; Ruberto, M.; Biondi, A.; Cascio, O.; Bertozzi, G.; et al. Heart rate variability as predictive factor for sudden cardiac death. *Aging* **2018**, *10*, 166–177. [CrossRef]
6. Dekker, J.M.; Crow, R.S.; Folsom, A.R.; Hannan, P.J.; Liao, D.; Swenne, C.A.; Schouten, E.G. Low Heart Rate Variability in a 2-Minute Rhythm Strip Predicts Risk of Coronary Heart Disease and Mortality from Several Causes. *Circulation* **2000**, *102*, 1239–1244. [CrossRef]
7. Jacobs, S.F. Optical heterodyne (coherent) detection. *Am. J. Phys.* **1988**, *56*, 235–245. [CrossRef]
8. Koukoulas, T.; Theobald, P.; Robinson, S.P.; Hayman, G.; Moss, B. Particle velocity measurements using heterodyne interferometry and Doppler shift demodulation for absolute calibration of hydrophones. *Proc. Meet. Acoust.* **2012**, *17*, 070022. [CrossRef]
9. Koukoulas, T.; Robinson, S.; Rajagopal, S.; Zeqiri, B. A comparison between heterodyne and homodyne interferometry to realise the SI unit of acoustic pressure in water. *Metrologia* **2016**, *53*, 891–898. [CrossRef]
10. Pinotti, M.; Paone, N.; Santos, F.A.; Tomasini, E.P. Carotid artery pulse wave measured by a laser vibrometer. In Proceedings of the Third International Conference on Vibration Measurements by Laser Techniques: Advances and Applications, Ancona, Italy, 16–19 June 1998; Volume 3411, pp. 611–616.
11. Morbiducci, U.; Scalise, L.; De Melis, M.; Grigioni, M. Optical Vibrocardiography: A Novel Tool for the Optical Monitoring of Cardiac Activity. *Ann. Biomed. Eng.* **2006**, *35*, 45–58. [CrossRef]
12. Scalise, L.; Cosoli, G.; Casacanditella, L.; Casaccia, S.; Rohrbaugh, J. The measurement of blood pressure without contact: An LDV-based technique. In Proceedings of the 2017 IEEE International Symposium on Medical Measurements and Applications (MeMeA), Rochester, MN, USA, 7–10 May 2017; pp. 245–250.
13. Scalise, L.; Morbiducci, U.; De Melis, M. A laser Doppler approach to cardiac motion monitoring: Effects of surface and measurement position. In Proceedings of the Seventh International Conference on Vibration Measurements by Laser Techniques: Advances and Applications, Ancona, Italy, 19–22 June 2006; Volume 6345, p. 63450.

14. De Melis, M.; Grigioni, M.; Morbiducci, U.; Scalise, L. *Optical Monitoring of Heartbeat, Modelling in Medicine and Biology*; WIT Press: Southampton, UK, 2005; pp. 181–190.

15. Donati, S.; Falzoni, L.; Merlo, S. A PC-interfaced, compact laser-diode feedback interferometer for displacement measurements. *IEEE Trans. Instrum. Meas.* **1996**, *45*, 942–947. [CrossRef]

16. Roos, P.A.; Stephens, M.; Wieman, C.E. Laser vibrometer based on optical-feedback-induced frequency modulation of a single-mode laser diode. *Appl. Opt.* **1996**, *35*, 6754–6761. [CrossRef]

17. Merlo, S.; Donati, S. Reconstruction of displacement waveforms with a single-channel laser-diode feedback interferometer. *IEEE J. Quantum Electron.* **1997**, *33*, 527–531. [CrossRef]

18. Beheim, G.; Fritsch, K. Range finding using frequency-modulated laser diode. *Appl. Opt.* **1986**, *25*, 1439–1442. [CrossRef]

19. Shinohara, S.; Yoshida, H.; Ikeda, H.; Nishide, K.; Sumi, M. Compact and high-precision range finder with wide dynamic range and its application. *IEEE Trans. Instrum. Meas.* **1992**, *41*, 40–44. [CrossRef]

20. De Groot, P.J.; Gallatin, G.M.; Macomber, S.H. Ranging and velocimetry signal generation in a backscatter-modulated laser diode. *Appl. Opt.* **1988**, *27*, 4475–4480. [CrossRef]

21. Özdemir, Ş.K.; Ito, S.; Shinohara, S.; Yoshida, H.; Sumi, M. Correlation-based speckle velocimeter with self-mixing interference in a semiconductor laser diode. *Appl. Opt.* **1999**, *38*, 6859–6865. [CrossRef] [PubMed]

22. Wang, W.; Grattan, K.; Palmer, A.; Boyle, W.J.O. Self-mixing interference inside a single-mode diode laser for optical sensing applications. *J. Light. Technol.* **1994**, *12*, 1577–1587. [CrossRef]

23. Cosoli, G.; Casacanditella, L.; Tomasini, E.; Scalise, L. Evaluation of Heart Rate Variability by means of Laser Doppler Vibrometry measurements. *J. Phys. Conf. Ser.* **2015**, *658*, 012002. [CrossRef]

24. Donati, S. Developing self-mixing interferometry for instrumentation and measurements. *Laser Photonics-Rev.* **2012**, *6*, 393–417. [CrossRef]

25. Perchoux, J.; Quotb, A.; Atashkhooei, R.; Azcona, F.J.; Ramírez-Miquet, E.E.; Bernal, O.; Jha, A.; Luna-Arriaga, A.; Yanez, C.; Caum, J.; et al. Current Developments on Optical Feedback Interferometry as an All-Optical Sensor for Biomedical Applications. *Sensors* **2016**, *16*, 694. [CrossRef]

26. Taimre, T.; Nikolić, M.; Bertling, K.; Lim, Y.L.; Bosch, T.; Rakić, A.D. Laser feedback interferometry: A tutorial on the self-mixing effect for coherent sensing. *Adv. Opt. Photonics* **2015**, *7*, 570–631. [CrossRef]

27. Hisatake, S.; Kitahara, G.; Ajito, K.; Fukada, Y.; Yoshimoto, N.; Nagatsuma, T. Phase-Sensitive Terahertz Self-Heterodyne System Based on Photodiode and Low-Temperature-Grown GaAs Photoconductor at 1.55 μm. *IEEE Sens. J.* **2012**, *13*, 31–36. [CrossRef]

28. Otsuka, K. Self-Mixing Thin-Slice Solid-State Laser Metrology. *Sensors* **2011**, *11*, 2195–2245. [CrossRef] [PubMed]

29. Mohr, T.; Breuer, S.; Blömer, D.; Simonetta, M.; Patel, S.; Schlosser, M.; Deninger, A.; Birkl, G.; Giuliani, G.; Elsäßer, W. Terahertz homodyne self-mixing transmission spectroscopy. *Appl. Phys. Lett.* **2015**, *106*, 061111. [CrossRef]

30. Donati, S.; Rossi, D.; Norgia, M. Single Channel Self-Mixing Interferometer Measures Simultaneously Displacement and Tilt and Yaw Angles of a Reflective Target. *IEEE J. Quantum Electron.* **2015**, *51*, 1–8. [CrossRef]

31. Bernal, O.D.; Zabit, U.; Bosch, T. Study of Laser Feedback Phase Under Self-Mixing Leading to Improved Phase Unwrapping for Vibration Sensing. *IEEE Sens. J.* **2013**, *13*, 4962–4971. [CrossRef]

32. Gao, Y.; Yu, Y.; Xi, J.; Guo, Q. Simultaneous measurement of vibration and parameters of a semiconductor laser using self-mixing interferometry. *Appl. Opt.* **2014**, *53*, 4256–4263. [CrossRef]

33. Kvitek, O.; Hendrych, R.; Kolská, Z.; Švorčík, V. Grafting of Gold Nanoparticles on Glass Using Sputtered Gold Interlayers. *J. Chem.* **2014**, *2014*, 1–6. [CrossRef]

34. Dean, P.; Lim, Y.L.; Valavanis, A.; Kliese, R.; Nikolić, M.; Khanna, S.P.; Lachab, M.; Indjin, D.; Ikonić, Z.; Harrison, P.; et al. Terahertz imaging through self-mixing in a quantum cascade laser. *Opt. Lett.* **2011**, *36*, 2587–2589. [CrossRef]

35. ISOMET. Available online: https://www.isomet.com/acousto_optics.html (accessed on 1 July 2021).

36. Capelli, G.; Bollati, C.; Giuliani, G. Non-contact monitoring of heartbeat using optical laser diode vibrocardiography. In Proceedings of the 2011 International Workshop on BioPhotonics, Parma, Italy, 8–10 June 2011; pp. 1–3.

37. ANALOG DEVICES. Available online: https://www.analog.com/media/en/technical-documentation/data-sheets/ad8232.pdf (accessed on 1 July 2021).

38. Villegas, A.; McEneaney, D.; Escalona, O. Arm-ECG Wireless Sensor System for Wearable Long-Term Surveillance of Heart Arrhythmias. *Electronics* **2019**, *8*, 1300. [CrossRef]

39. Donati, S.; Giuliani, G.; Merlo, S. Laser diode feedback interferometer for measurement of displacements without ambiguity. *IEEE J. Quantum Electron.* **1995**, *31*, 113–119. [CrossRef]

40. Donati, S.; Norgia, M. Self-Mixing Interferometry for Biomedical Signals Sensing. *IEEE J. Sel. Top. Quantum Electron.* **2013**, *20*, 104–111. [CrossRef]

41. De Mul, F.F.M.; Van Spijker, J.; Van Der Plas, D.; Greve, J.; Aarnoudse, J.G.; Smits, T.M. Mini laser-Doppler (blood) flow monitor with diode laser source and detection integrated in the probe. *Appl. Opt.* **1984**, *23*, 2970–2973. [CrossRef]

42. Hast, J.; Myllylä, R.; Sorvoja, H.; Miettinen, J. Arterial pulse shape measurement using self-mixing effect in a diode laser. *Quantum Electron.* **2002**, *32*, 975–980. [CrossRef]

43. Arasanz, A.; Azcona, F.; Royo, S.; Jha, A.; Pladellorens, J. A new method for the acquisition of arterial pulse wave using self-mixing interferometry. *Opt. Laser Technol.* **2014**, *63*, 98–104. [CrossRef]

44. Scalise, L.; Morbiducci, U. Non-contact cardiac monitoring from carotid artery using optical vibrocardiography. *Med. Eng. Phys.* **2008**, *30*, 490–497. [CrossRef]

45. Riva, C.; Ross, B.; Benedek, G.B. Laser Doppler measurements of blood flow in capillary tubes and retinal arteries. *Investig. Ophthalmol.* **1972**, *11*, 936–944.

46. Norgia, M.; Donati, S.; D'Alessandro, D. Interferometric measurements of displacement on a diffusing target by a speckle tracking technique. *IEEE J. Quantum Electron.* **2001**, *37*, 800–806. [CrossRef]

47. Giuliani, G.; Bozzi-Pietra, S.; Donati, S. Self-mixing laser diode vibrometer. *Meas. Sci. Technol.* **2002**, *14*, 24–32. [CrossRef]

48. Zabit, U.; Bernal, O.D.; Bosch, T. Self-Mixing Laser Sensor for Large Displacements: Signal Recovery in the Presence of Speckle. *IEEE Sens. J.* **2013**, *13*, 824–831. [CrossRef]

49. Nikolić, M.; Jovanović, D.P.; Lim, Y.L.; Bertling, K.; Taimre, T.; Rakić, A.D. Approach to frequency estimation in self-mixing interferometry: Multiple signal classification. *Appl. Opt.* **2013**, *52*, 3345–3350. [CrossRef] [PubMed]

50. Cosoli, G.; Casacanditella, L.; Tomasini, E.P.; Scalise, L. The non-contact measure of the heart rate variability by laser Doppler vibrometry: Comparison with electrocardiography. *Meas. Sci. Technol.* **2016**, *27*, 065701. [CrossRef]

51. Kim, H.-G.; Cheon, E.-J.; Bai, D.-S.; Lee, Y.H.; Koo, B.-H. Stress and Heart Rate Variability: A Meta-Analysis and Review of the Literature. *Psychiatry Investig.* **2018**, *15*, 235–245. [CrossRef]

52. Giuliani, G.; Norgia, M.; Donati, S.; Bosch, T. Laser diode self-mixing technique for sensing applications. *J. Opt. A Pure Appl. Opt.* **2002**, *4*, S283–S294. [CrossRef]

53. De Melis, M.; Morbiducci, U.; Scalise, L. Identification of cardiac events by Optical Vibrocardiograpy: Comparison with Phonocardiography. In Proceedings of the 2007 29th Annual International Conference of the IEEE Engineering in Medicine and Biology Society, Lyon, France, 23–26 August 2007; Volume 2007, pp. 2956–2959.

54. Rawankar, A.; Urakawa, J.; Shimizu, H.; You, Y.; Terunuma, N.; Aryshev, A.; Honda, Y. Design studies on compact four mirror laser resonator with mode-locked pulsed laser for 5 μm laser wire. *Nucl. Instrum. Methods Phys. Res. Sect. A Accel. Spectrom. Detect. Assoc. Equip.* **2013**, *700*, 145–152. [CrossRef]

55. You, Y.; Urakawa, J.; Rawankar, A.; Aryshev, A.; Shimizu, H.; Honda, Y.; Yan, L.; Huang, W.; Tang, C. Measurement of beam waist for an optical cavity based on Gouy phase. *Nucl. Instrum. Methods Phys. Res. Sect. A Accel. Spectrom. Detect. Assoc. Equip.* **2012**, *694*, 6–10. [CrossRef]

56. Aarathy, E.R.; Rawankar, A.; Kumar, N.S. Measurement of Parameters of Frequency-Locked Two-Mirror Laser Resonator. In *Lecture Notes in Electrical Engineering*; Springer: Singapore, 2018; Volume 472, pp. 277–286.

57. Rawankar, A.A.; Terunuma, N.; Urakawa, J.; Akagi, T.; Aryshev, A.S.; Honda, Y.; Jehanno, D. Pulsed green laser wire system for effective inverse Compton scattering. In Proceedings of the IBIC 2014—3rd International Beam Instrumentation Conference, Monterey, CA, USA, 14–18 September 2014.

58. Donati, S.; Norgia, M. Overview of self-mixing interferometer applications to mechanical engineering. *Opt. Eng.* **2018**, *57*, 051506. [CrossRef]